

Title
Document Number
Issue
Issue Date
CI Number
DRL Number
Model
As-Run Number
Data Classification
Category
(Approval, Review, Information)
Export Classification

Executive Summary

D4DONE-OHB-RP-0002

01

15.07.2024

Public

DE Number: US Number:

| Name | Responsibility | Signature/Date |
|--------------|-----------------|----------------|
| prepared by | | |
| D4D-ONE Team | | |
| checked by | | |
| B. Lockett | MMPP Engineer | |
| | | |
| approved by | | |
| B. Ganzer | Project Manager | |



Belstead



Document Change Record

| Issue | Date | Change Description/Reason (Ref.) | Page/Chapter Affected |
|-------|------------|----------------------------------|-----------------------|
| 01 | 15.07.2024 | Initial Issue | all |

Table of Contents

| | | |
|----------|---|-----------|
| 1 | INTRODUCTION | 7 |
| 2 | REFERENCES | 7 |
| 2.1 | Applicable Documents | 7 |
| 3 | CRITICAL PLATFORM OPTICS AND ELECTRONICS | 8 |
| 3.1 | Selection of Test Items | 8 |
| 4 | TEST RESULTS AND MODEL UPDATES | 9 |
| 4.1 | Star Tracker | 9 |
| 4.1.1 | Model Updates | 12 |
| 4.1.2 | Re-entry Simulations | 14 |
| 4.1.3 | Modelling Conclusions | 16 |
| 4.2 | Batteries | 16 |
| 4.2.1 | Model Updates | 22 |
| 4.2.2 | Re-Entry Simulations | 25 |
| 4.2.3 | Modelling Conclusions | 28 |
| 4.3 | Electronic Equipment | 29 |
| 4.3.1 | Model Updates | 37 |
| 4.3.2 | Re-Entry Simulations | 40 |
| 4.3.3 | Modelling Conclusions | 41 |
| 5 | RECOMMENDATIONS AND FUTURE WORK | 42 |
| 5.1 | Star Tracker – Lessons Learned | 42 |
| 5.2 | Batteries – Lessons Learned | 42 |
| 5.3 | Electronics – Lessons Learned | 42 |
| 5.4 | Modelling | 43 |
| 5.4.1 | Model Construction | 43 |
| 5.4.2 | Required DRAMA Upgrades | 46 |
| 5.4.3 | DRAMA Models | 47 |
| 5.5 | DIVE recommendations | 48 |
| 5.6 | Recommendations for Future Work | 49 |
| 5.6.1 | Testing and Modelling | 49 |
| 5.6.2 | Design Ideas to Improve the Equipment Demise | 49 |

List of Tables

| | |
|--|----|
| Table 2-1: Applicable Documents..... | 7 |
| Table 3-1: Test Item Trade Space..... | 9 |
| Table 4-1: Updated Large Star Tracker Model..... | 13 |
| Table 4-2: Battery Model with GFRP..... | 22 |
| Table 4-3: Updated Battery Models..... | 24 |
| Table 4-4: Server-Type Electronics Box Model..... | 38 |
| Table 4-5: Updated Stack-Type Electronics Box Model..... | 39 |
| Table 4-6: DRAMA Equivalent Metal GFRP Model..... | 41 |
| Table 5-1: Material Model Updates..... | 43 |
| Table 5-2: Star Tracker Model Recommendations..... | 44 |
| Table 5-3: Battery Model Recommendations..... | 44 |
| Table 5-4: Electronics Model Recommendations..... | 45 |

List of Figures

| | |
|---|----|
| Figure 4-1: JOP ASTRO APS Imaging System..... | 10 |
| Figure 4-2: Star Tracker Test Sample configurations..... | 10 |
| Figure 4-3: Screenshot from S5 video at 20 s (left), 40 s (centre) and 300 s (left) test time..... | 10 |
| Figure 4-4: Images from HD-video of test S4 after test times of 158 s (left), 443 s (centre left), 466 s (centre right) and 474 s (right, directly before the end of the test)..... | 11 |
| Figure 4-5: Images from InfraTec-IR-camera of test S4 after test times of 158 s (left), 443 s (centre left), 466 s (centre right) and 474 s (right, directly before the end of the test)..... | 11 |
| Figure 4-6: Images from HD-camera at 15s, 180s, 230s and 247s..... | 12 |
| Figure 4-7: Images from InfraTec IR-camera at 15s, 180s, 230s and 247s..... | 12 |
| Figure 4-8: SAMj Viewer Images of Updated Star Tracker Model..... | 14 |
| Figure 4-9: SAMj Viewer Images of Updated Small Star Tracker Model..... | 14 |
| Figure 4-10: Landed Fragment Count for Large Star Tracker..... | 14 |
| Figure 4-11: Casualty Area from Large Star Tracker..... | 14 |
| Figure 4-12: Landed Mass from Large Star Tracker..... | 15 |
| Figure 4-13: PADRE Probabilities Key..... | 15 |
| Figure 4-14: Landed Fragment Number from Small Star Tracker..... | 15 |
| Figure 4-15: Casualty Area from Small Star Tracker..... | 15 |
| Figure 4-16: Landed Mass from Small Star Tracker..... | 16 |
| Figure 4-17: ABSL Single Battery Cell Test Sample..... | 17 |
| Figure 4-18: ABSL Battery Module Test Sample, 0° Angle of Attack..... | 17 |
| Figure 4-19: ABSL Battery Module Test Samples, 45° Angle of Attack..... | 17 |

Figure 4-20: Screenshot from HD video at 180 s (left), 220 s (centre) and 400 s (right) test time 18

Figure 4-21: Images from InfraTec IR-camera of test S7 at 180 s (left), 220 s (centre) and 400 s (right) test time 18

Figure 4-22: Images from HD video of test S7 at 435 s (left), 500 s (centre) and 548 s (right) test time 19

Figure 4-23: Images from InfraTec IR camera of test S7 at 435 s (left), 500 s (centre) and 548 s (right) test time 19

Figure 4-24: Images from HD-video of test S8 at 195 s (left), 260 s (centre) and 315 s (left) test time..... 20

Figure 4-25: Images from InfraTec IR-camera of test S8 at 195 s (left), 260 s (centre) and 315 s (left) test time 20

Figure 4-26: IR images of tests battery module tests with 0.3 Hz and 2.0 Hz rotation rate shortly before first cells become lose..... 21

Figure 4-27: Test at 0.3 Hz - Still Frame (left) and IR (right) after 140 s, 275 s, 294 s test time 21

Figure 4-28: Test at 2 Hz Still Frame (left) and IR (right) after 120 s 170 s 200 s test time..... 21

Figure 4-29: SAMj Viewer Images of Battery Model 23

Figure 4-30: Battery Fragmentation Schematic..... 23

Figure 4-31: Nested Layers in Fragmentation Model 23

Figure 4-32: Updated Battery Model 24

Figure 4-33: Landed Object Number from Baseline Battery Model 25

Figure 4-34: Landed Mass from Baseline Battery Model 25

Figure 4-35: Landed Fragments from Layer-by-layer Battery Fragmentation..... 26

Figure 4-36: Landed Mass from Battery Fragmenting Layer-by-Layer 26

Figure 4-37: Fragment Count from Updated Battery Model Simulation 27

Figure 4-38: Landed Mass from Updated Battery Model Simulation 27

Figure 4-39: Fragment Count from 10kg Battery Model Simulation 27

Figure 4-40: Landed Mass from 10kg Battery Model Simulation 27

Figure 4-41: Fragment Count from 20kg Battery Model Simulation 28

Figure 4-42: Landed Mass from 20kg Battery Model Simulation 28

Figure 4-43: Fragment Count from 30kg Battery Model Simulation 28

Figure 4-44: Landed Mass from 30kg Battery Model Simulation 28

Figure 4-45: Fragment Count from 30kg Equivalent Battery Model Simulation 29

Figure 4-46: Landed Mass from 30kg Equivalent Battery Model Simulation 29

Figure 4-47: PCB, 0° Angle of Attack 30

Figure 4-48: PCB, 45° Angle of Attack 30

Figure 4-49: Enmap PCB Sample 30

Figure 4-50: PD Board Sample 30

Figure 4-51: BCM Sample 30

Figure 4-52: PCDU Board Sample 30

Figure 4-53: Delamination of GFRP layers at the leading after 5 s (left) and bending of the board around the sample holder after 25 s; Melting of EnMap board at the middle and just before the of the test (right)..... 31

Figure 4-54: Sequence of images from PD Test 31

Figure 4-55: Test S14 at test times of 35 s, 45 s, 170 s and 260 s 32

Figure 4-56: Test S13 after 60 s test time (left image), 90 s and 300 s 32

Figure 4-57: Stacked BCM Test at test times of 60s, 100 s, 120 s 33

Figure 4-58: Stacked BCM Test at test times of 135 s and 240 s 33

Figure 4-59: EnMap (top) and PD (bottom) board sections at the end of 100 kW/m² (left) and 200 kW/m² (centre) heat flux steps and during full demise at 300 kW/m² (right) 34

Figure 4-60: EnMap (left) and PD (right) board sections after the tests, still mounted in L2K 35

Figure 4-61: Images from video cameras of EnMap board test after 15 s (left), 64 s (centre) and 130 s (right) test time 35

Figure 4-62: Images from video cameras of PD board test after 60 s (left), 108 s (centre) and 172 s (right) test time 36

Figure 4-63: BCM after cover plate removal (left), failing of housing (centre) and board remains just before the end of the test (right) 36

Figure 4-64: SAMj Viewer of Stack-Type Electronics Box Housing and Modules 40

Figure 4-65: SAMj Viewer of Stack-Type Electronics Box Cards and Internals 40

Figure 4-66: Fragment Count from Server-Type Electronics Box 40

Figure 4-67: Landed Mass from Server-Type Electronics Box 40

Figure 4-68: Fragment Count from Stack-Type Electronics Box 41

Figure 4-69: Landed Mass from Stack-Type Electronics Box 41

Figure 5-1: Star Tracker Model Example 44

Figure 5-2: Battery Model Example 45

Figure 5-3: Electronics Box Model Example 46

1 INTRODUCTION

The re-entry of space systems into the earth atmosphere can contain fragments which are able to survive the loads and heat experienced during re-entry into the atmosphere. These fragments will have a probability to cause harm or damage to humans and the environment. The casualty risk is driven by the number and size of re-entering fragments. Design for Demise techniques have been developed in order to reduce the casualty risks on Earth.

Already numerous studies and projects have been performed in order to gain better understanding of re-entry processes and to assure that more spacecraft fragments demise during the re-entry. Yet, substantial knowledge gaps on the demise and fragmentation processes of various components remain to be closed.

The objective of this activity is to enhance the knowledge on the demise of optical and electrical equipment of satellite platforms in order to establish validated re-entry models. For this purposes equipment potentially causing re-entry risks, as star trackers, batteries modules and electronic equipment is analysed and investigated in on-ground demise tests in representative environment.

2 REFERENCES

2.1 Applicable Documents

This document shall be read in conjunction with documents listed hereafter, which form part of this document to the extent specified herein. In case of a conflict between any provisions of this document and the provisions of the documents listed hereafter, the content of the contractually higher document shall be considered as superseding.

Table 2-1: Applicable Documents

| AD No. / Title | Doc. No. | Issue |
|--|---------------------------|-------|
| [AD01] Statement of Work Platform Optics and Electronic Equipment Demise | ESA-TRP-TECSYE-SOW-023687 | 1.1 |

3 CRITICAL PLATFORM OPTICS AND ELECTRONICS

To gather information on the equipment used on LEO satellite platforms, the literature review was approached from two sides. In a first step past, current and future LEO satellites platforms that are mainly used in earth observation, telecom and constellations were identified and quantified on a high level. Further the equipment products used on these platforms was identified mostly based on public information as well as on internal data bases. From the gathered information the most commonly applied products and suppliers were extracted. The part and materials used in these products were determined where possible.

Since 2010 more than 70+ different satellite platforms (> 200 kg) are operational in LEO. They represent most of the currently 4000+ satellites in LEO. The most commonly used star tracker brands used in EO satellites and telecom satellites, individual and constellations, are as far as it could be determined:

- Sodern more than 700 star tracker in orbit (mostly Aurigas in OneWeb)
- Jena-Optronik sold 400 star tracker , more than 100 in orbit (GEO, MEO, LEO)
- Leonardo, e.g. SpaceStar in Iridium Next (80+)
- DTU (15+ missions)

In total 60+ star tracker types from 20+ suppliers for small, medium and large satellites are currently available on the global market. The star tracker masses range from 40g to 4kg. The material assessment was performed for heavier star trackers with a mass well above 200g. The main materials used in star trackers are aluminium and titanium alloys. The mass of each component and material may vary with specific star tracker and its size. In the future smaller star tracker (< 1kg) for small satellites and constellations will be more dominant in numbers. These star trackers are usually based on heritage but are optimized and adapted for cost driven design and mass production. However, in principle they are comprised of the same components as larger star trackers.

Two of the main suppliers providing batteries for LEO satellite platforms are ABSL (now part of EnerSys) and SAFT:

- ABSL: 340+ spacecraft in orbit
- SAFT: VES16 cells 200+ satellite equipped with its lithium-ion battery

The ABSL batteries are based on small cells (D20mm x 70mm). The cells are arranged in cell array or block configurations. The cell blocks then comprise battery modules of different standard sizes and form factors. The materials of the battery module outer structure includes mainly aluminium. For the inner cells blocks glass fibre reinforced plastic sheets (GFRP) are used to isolate the cells and take the structural load. This material is machined with counter bored holes into which the cells are bonded. The cells are glued, or a good thermal and structural joint. The block assembly, comprising the cells and upper and lower GFRP plates is highly rigid.

Electronics boxes represent different equipment used on satellites on platform and equipment level. On platform level typical electronic boxes are on board computers (OBC), Remote Terminal Units (RTU) and power conditioning and distribution units (PCDU). This equipment is supplies by various suppliers in numerous different design, form factors and sizes. The structure of the electronics boxes are usually made of aluminium alloys. The main components however are PCB often made of GFRP, which are equipped with space grade (hard rad) electronical parts. The material composition and distribution used for these electronical parts are difficult to determine, as it depends also on the specific purpose of the PCB. It is safe to assume that copper is one of the main materials. Typical elements on PCB are:

- Resistors and Capacitors
- Diodes and Microcircuits / IC
- Processors and SRAM

3.1 Selection of Test Items

The following trade-off and selection criteria are defined for the selection of test items:

- Items characteristics that will be needed to verify the events of interest in the demise tests, observed in the simulations (e.g. demise and fragmentation process)
- Equipment level tests able to verify fragmentation / demise process over material level tests to verify material properties.

- Availability of test samples (i.e. procured/acquired within the study timeframe).
- Suitability of test sample geometries for the demise tests in the foreseen test facilities

The following table summarizes the trade space for test items.

Table 3-1: Test Item Trade Space

| Equipment | Critical Elements | Events of interest | Equipment level tests | Availability | Suitability of geometries |
|-------------------|--|---|-----------------------|--|--|
| Star Tracker | Titanium made the focal plane array housing and the optical barrel | Has not been tested before Behaviours of critical parts Fragmentation of unit | Feasible | Jenaoptronik Current generation of ASTRO APS imaging system | ok |
| Batteries | GFRP Sheets Larger Cells | Behaviours of critical parts Fragmentation of unit | Feasible | ABSL small single cells & 4x4 modules | Single Cell ok Small Modules ok |
| Electronics Boxes | PCB Cards (GFRP) | Behaviours of critical parts Fragmentation of unit | Feasible | OHB PCDU / PPDU BCM Unpopulated PCBs | Cards and modules have to be cut to size |

4 TEST RESULTS AND MODEL UPDATES

The test activities involved the investigation of electronic and optics components, that were identified as critical components for the demisability of a spacecraft in this study. These component types are part of star trackers, batteries, and electronic boards. The following test samples are to be tested in this activity:

- Star tracker: Jena Optronik ASTRO APS imaging system and simplified mock-ups
- Batteries: ABSL batteries and battery modules
- Electronics boards: OHB-manufactured LEO populated PCB's

The tests were performed in two plasma wind tunnel test campaigns in DLR LK2 facility. During the first campaign tests with static set-up were performed. During the second campaign test with dynamic (rotational) set-up were performed. The result of the first campaign were evaluated before the start of the second campaign, so that necessary adjustments to predictive simulations and resulting test conditions could be made.

4.1 Star Tracker

An ASTRO APS Lens Assembly was provided by Jena Optronik. It is complemented by simple mock-up parts for the focal plane assembly (wedge ring, Adapter Plate, Intermediate Plate). The Lens Assembly contains three different lenses. In order to simplify the geometry and aligned the test data collection with the modelling and simulation mock-up assemblies were derived from the original components of the ASTRO APS Imaging System shown in Figure 4-1. The Full-Size Mock-up has the same envelope size as the original unit. The stepped lens tube was simplified as to a cylinder as shown in Figure 4-2. The Adapter Plate and Intermediate Plate were modified to form a simple two part box as depicted in Figure 4-2.

In addition a half sized mock-up is also used for the test in order to investigate the full demise process. The Half-Size Mock-up has the same geometry and components as the full-size mock-up but with reduced dimensions as shown in Figure 4-2.

Two static tests were done with the two full-size mock-up samples of the star tracker. The first of these tests was started at 400 kW/m². After approximately 3 minutes test time and thermal equilibrium of the sample for a considerable duration, the distance to the nozzle was reduced to 200 mm to achieve a higher heat flux (500 kW/m²). After 34 s test time at this condition, the sample holder failed, as the threaded bolt for mounting the sample to the shaft of the rotation device of L2K had melted.

The second test with a full-size mock-up was directly started at 500 kW/m². Already after approximately 15 s test time, the front face of the cylinder section begins to melt. It is assumed that the impingement of the shock of the cylinder ring and the mounting box is a major driver for this behaviour. It is also interesting as despite the failure of the holder in the first test, the sample still stood at this heat flux condition for over 30 s without the cylinder face beginning to melt. Presumably, the cause for this is that during the phase of the first test at 400 kW/m², an oxide layer formed around the sample, while the time for this was too short in the second test.



Figure 4-1: JOP ASTRO APS Imaging System



Figure 4-2: Star Tracker Test Sample configurations

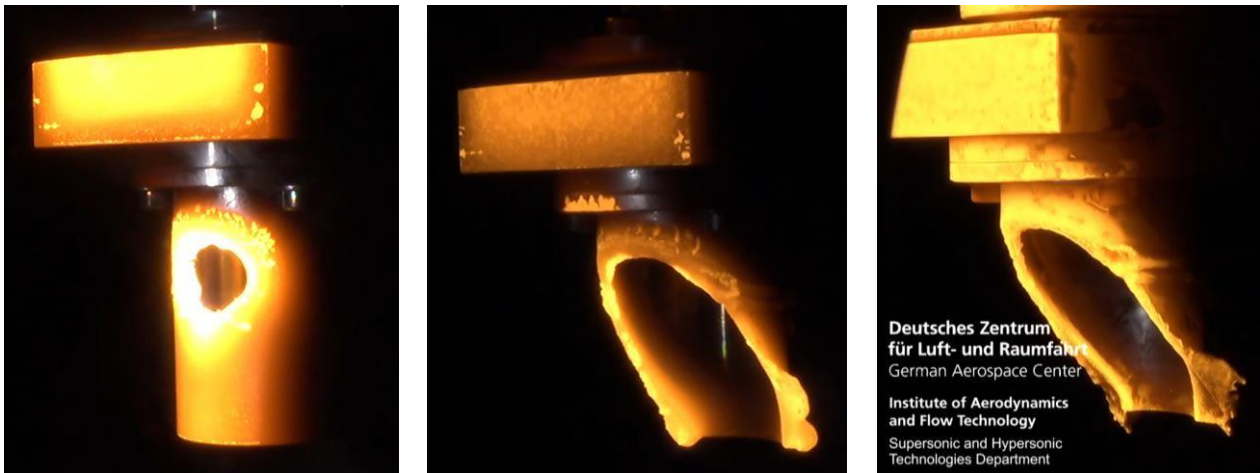


Figure 4-3: Screenshot from S5 video at 20 s (left), 40 s (centre) and 300 s (left) test time

Two tests were also conducted with the half-size mock-ups. The dimensions of the half-size mock-ups were reduced by the factor of two, in order to increase local heat fluxes and gain a better understanding of the demise behaviour. In the first test (S3) the sample was tested at four heat flux levels from 200 to 350 kW/m² (on 50 mm heat flux probe) for a total test time of 385.5 s. No demise was reached in this test, as the screws fixating the reducer to the sample failed after approximately 34 s at the highest heat flux level. Still, thermal equilibrium was reached at each condition. For the second test, the total test duration was 474.8 s at heat flux levels of 400 kW/m, 500 kW/m² and 580 kW/m². After thermal equilibrium had been reached at the first two

conditions for a considerable time, demise was quickly achieved after the sample was exposed to the highest heat flux.

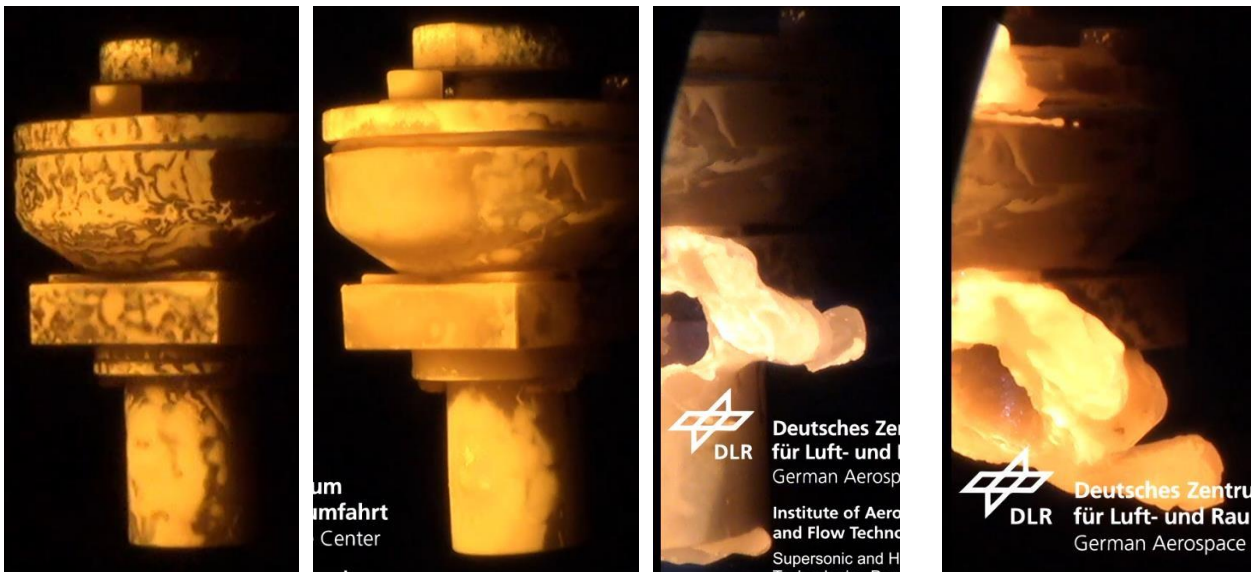


Figure 4-4: Images from HD-video of test S4 after test times of 158 s (left), 443 s (centre left), 466 s (centre right) and 474 s (right, directly before the end of the test)

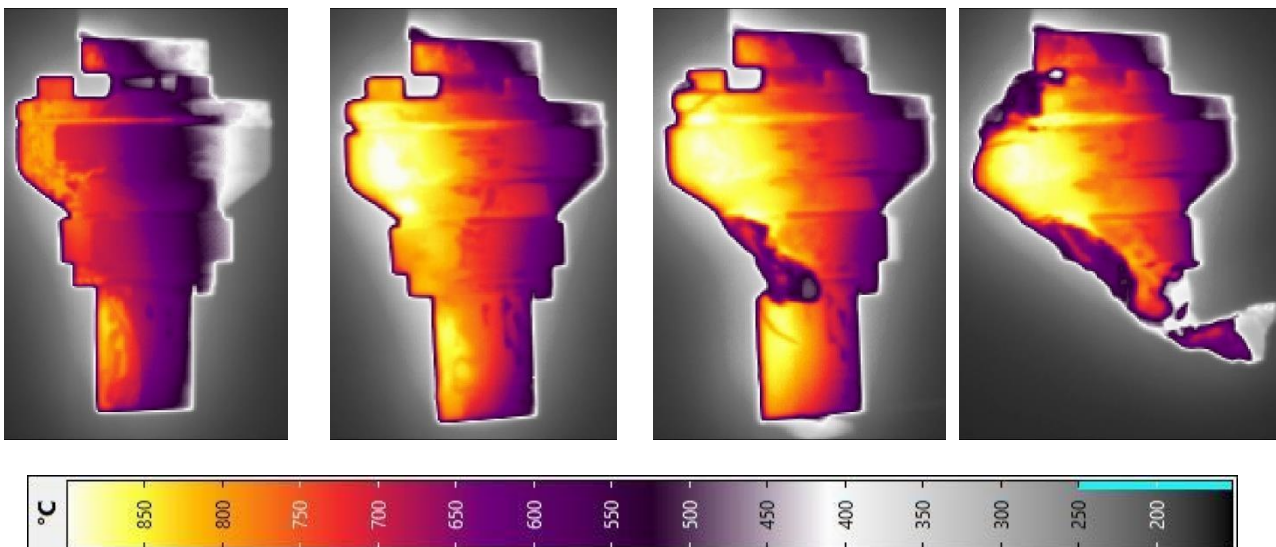


Figure 4-5: Images from InfraTec-IR-camera of test S4 after test times of 158 s (left), 443 s (centre left), 466 s (centre right) and 474 s (right, directly before the end of the test)

One test was done with the JOP Astra APS lens assembly. In this test original star tracker hardware was investigated. The test was started at a heat flux level of 400 kW/m² and later at 500 kW/m² heat flux level. The test had a total duration of 248.5 s and was continued until the demise of the sample was reached. Similar to the full-size mock-up, substantial heating at the impingement location of the shock from the mounting box was observed early in the experiment. Furthermore, strong heating could also be seen at the lower rim of the lens tube. Comparably to the mock-up test, the heating rate of the sample was quite low with the heat propagating to the other sections of the sample quite slowly.

In addition to that, it also has to be noted that for the lens tube sample, a certain portion of energy intake into the sample goes into the heating and consecutive melting of the glass lenses, which have a considerable thermal mass. From 100 s test time onwards, it can be observed, that molten material from the lens begins to flow out of the bottom of the lens tube, as illustrated in the top right images of Figure 4-6 and Figure 4-7.

Over the next 100 s, this state continues. Molten lens material flows out of the sample, which slowly increases to heat up with the maximum temperatures in the hot spots of the shock impingement and the rim remaining constant.

After 201 s test time, it was decided to move the sample closer to the nozzle and increase the heat flux level to speed up the demise process. Consequently, the heating rate of the sample as well as the melting and outflow of the lens glass material rose. The first signs of melting of the housing can be observed after approximately 210 s test time, at the rim of the lens tube and the head of the screws fixating the lens tube to the focal plane box. Soon after that (about 5 to 10 s later), it appears that the lenses inside have completely melted. While some of the glass material is still attached to the rim for some time, the outflow of new material seems to be stopping at this point, indicating that the lenses are gone.

At the same time, the melting of the housing rapidly picks up. It appears that during the previous part of the experiment, a significant portion of the energy intake into the sample goes into the heating and melting of the lenses, which thus act as a heat sink. After they are gone, the demise process of the housing is strongly accelerated, with a gap being melted in the rim first and then a hole appearing at the impingement location of the shock from the box/cylinder disc. Only about 15 s later, the housing has mostly demised and the test was stopped.



Figure 4-6: Images from HD-camera at 15s, 180s, 230s and 247s

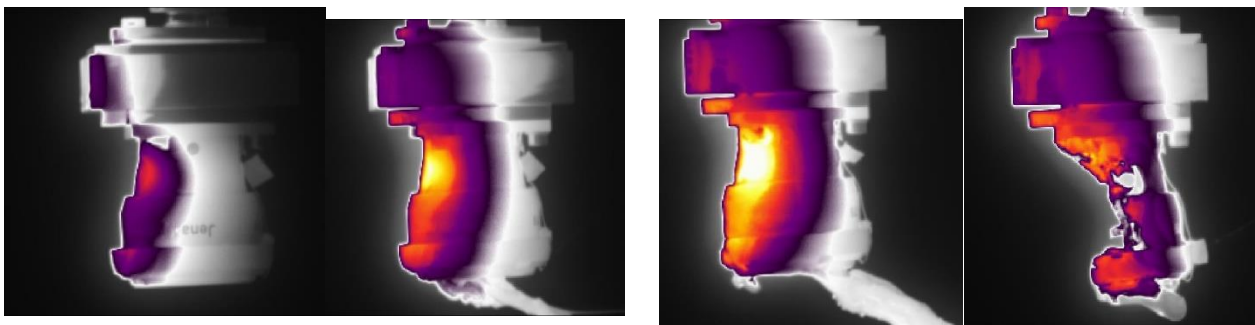


Figure 4-7: Images from InfraTec IR-camera at 15s, 180s, 230s and 247s

Demise of the star tracker samples was not achieved in both dynamic tests. The threads borings in the Intermediate Plate, holding the Lens Tube (cylinder part) were manufactured with helicoils. The helicoils failed early in the tests at the first heat flux level. Consequently, the samples fell off before any melting was observed.

4.1.1 Model Updates

In order to produce a reasonable model of a star tracker, some assessment of the parts is needed. In previous work (PADRE, D4D-CONT), star trackers were modelled with an aluminium housing and a titanium barrel for the lenses. In this activity, two titanium parts were modelled as both the barrel and the focal plane housing are titanium. This resulted in two landed parts being predicted, and an increase in the assessed casualty risk. The construction of the Jena Optronik star tracker has all the titanium parts together in order to minimise any thermal expansion effects, and the static tests showed that there was no separation of these parts. Therefore, it is considered reasonable to revert to the previous models where a single titanium part is considered. The size of this part is likely to increase as it has to cover the barrel and the focal plane housing.

From the test rebuilding, the titanium material performance is considered to be good. This is consistent with the data from a number of previous campaigns (D4D-CONT, CHARDEM, SCORED), and consolidates the current titanium material model. A glass material model is also needed in order to model the lenses. The test suggests that the glass used within star trackers is designed to be radiation hardened, and is therefore significantly more demisable than fused silica. The test results suggest that the viscosity of the glass at the point that it is being released is consistent with that of borosilicate glass, and that the glasses should be released from the titanium barrel before the onset of melt of the barrel. On the assumption that the molten glass flowed from the part which was in contact with the hot titanium barrel, it is reasonable to release the glass when the barrel reaches a temperature of 1500°C (titanium melt could be used for conservatism). It is reasonable to assume that the bulk glass is cold as the thermal conductivity is low.

The more difficult part of the model to assess is the application of a suitable length scale in order to capture the heating to the star tracker. There are a number of ways in which this could be applied:

- The star tracker barrel is modelled as a single titanium cylinder, but with the application of a heat flux scale to account for the length scale increase. This is the simplest model, but also the least conservative.
- The star tracker is modelled as a set of titanium cylinders of differing thickness and diameters in order to reasonably represent the geometry of the real unit. This allows fragmentation of the unit, but it will be reasonably difficult to manipulate in DRAMA as it has multiple parts which need moving separately. This could be mitigated by use of an overall aluminium housing for the unit to capture the base and the baffle.

The first stage is to attempt to capture the correct length scales by modelling the barrel as a set of titanium cylinders of differing radii. The critical aspect here is the thickness of the discs, although it should be noted that the melting of the edge of the cylinder is partially due to the fixed orientation of the test object. The model has also been adapted to be closer to the Jena Optronik star tracker which was tested. In order to maintain the mass at 1.5kg, a larger unit has been used than the ASTRO APS model tested. A basic scaling of the geometry and mass has been used. The updated large star tracker model is given in Table 4-1, and is shown in Figure 4-8. A factor 5 scaling has been used for the small star tracker. Images of this updated model are shown in Figure 4-9.

Table 4-1: Updated Large Star Tracker Model

| Component | Material | Mass (kg) | Colour | Notes |
|---|--------------|--------------|--------|--|
| Baffle | Aluminium | 0.35 | Cyan | Connected to housing |
| Optical Barrel Four concentric rings | Titanium | 0.2 | Orange | Contains lenses Connected to housing Connected to FPA No separation allowed |
| Housing | Aluminium | 0.34 | Green | Contains FPA, PCB Connected to baffle, optical barrel |
| Lens | Borosilicate | 0.02 (each) | Blue | Multiplicity used – 7 lenses Nested in optical barrel |
| Focal Plane Assembly | Titanium | 0.12 | Pink | Contains focal plane internals Connected to optical barrel |
| Focal Plane Internals | Aluminium | 0.033 (each) | Yellow | Multiplicity used – 3 objects Nested in FPA |
| PCB | GFRP | 0.25 | Green | Nesting in housing |

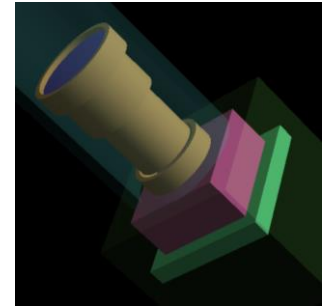
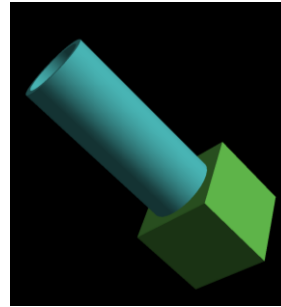
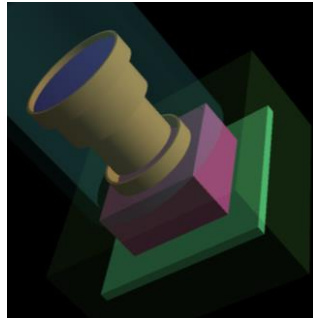
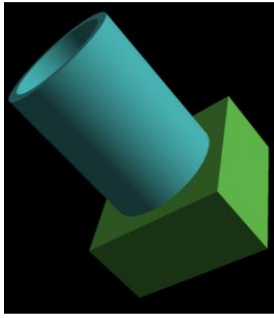


Figure 4-8: SAMj Viewer Images of Updated Star Tracker Model

Figure 4-9: SAMj Viewer Images of Updated Small Star Tracker Model

4.1.2 Re-entry Simulations

The preliminary simulations before the test were updated using the findings from the testing and rebuilding work. These simulations are again performed using the SAMj tool within the stochastic PADRE framework. This allows a comprehensive uncertainty model to be applied which covers all the aspects detailed within the DIVE document. The latest available version of the ESTIMATE database has also been applied, with improvements which have been observed in more recent test activities.

The large star tracker demonstrates a reduction in the casualty risk relative previous analysis, which is due to the capturing of the shorter length scales on the titanium star tracker, and ensuring that there is no separation between the optical barrel and the focal plane array. One titanium part lands in almost all simulations, regardless of release altitude, with additional casualty risk from the PCB, which lands approximately 75% of the time. This is shown as a function of altitude in Figure 4-10. The blue reaching the bottom shows that, very occasionally, the star tracker demises fully, but that this happens less than 5% of the time. For release altitudes under 60km, the baffle, and even the housing, can also land. In no case do multiple titanium parts land, even though this is possible the way the model is constructed.

This results in a casualty area of a little under 1m² for the majority of release altitude, as shown in Figure 4-11. It should be noted that this includes both the casualty area from the titanium parts (~0.5m²) and the PCB (~0.4m²).

The landed mass is actually slightly larger than in previous analysis as the larger titanium part is less demised than the two smaller parts modelled in that case. The PCB is about 150g, and the landed titanium parts about 600g, which includes lenses in most cases. This is reasonably constant at release altitudes above 70km, as shown in Figure 4-12

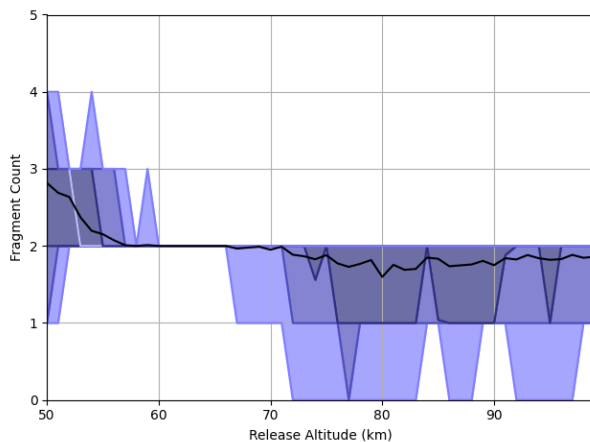


Figure 4-10: Landed Fragment Count for Large Star Tracker

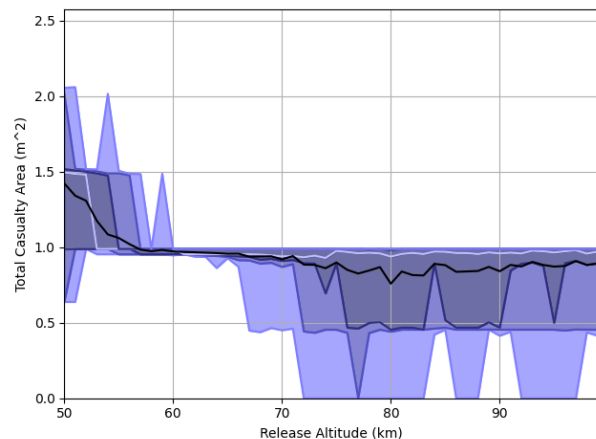


Figure 4-11: Casualty Area from Large Star Tracker

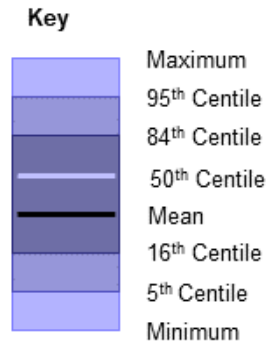
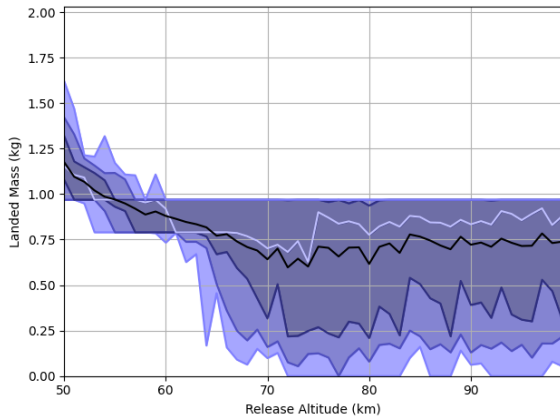


Figure 4-12: Landed Mass from Large Star Tracker

Figure 4-13: PADRE Probabilities Key

The small star tracker also shows a significant reduction in the number of landed objects, and the casualty area. This is again due to the titanium parts being held together such that not more than one titanium part can impact the ground. Figure 4-14 shows that, for all release altitudes above 65km, the expected number of ground impacts is below 1, and there is a sweet spot between 68km and 76km release altitude, where the median case shows complete demise of the star tracker. This suggests that there is a large benefit in the use of smaller star trackers from a demise point-of-view. It is also interesting to note that the 50g PCB does not provide a casualty risk in any of the simulations. This is due to its being under 15J impact energy as it is a low ballistic coefficient part.

The casualty area is shown in Figure 4-15, and shows that the risk is around 0.2m² for a release between 68km and 78km. There is a slight increase for earlier releases. In practice, this may be a conservative assessment as the star trackers are on the outside of the spacecraft and will receive some heating whilst attached to the spacecraft before they are released.

The mean landed mass from the star tracker is consistent with the Task 1 analysis, with the expected value being between 50g and 100g for most release altitudes, with a slightly lower minimum between 66km and 76km. This is shown in Figure 4-16.

This analysis confirms that star trackers should be included as a critical item in the casualty risk budget, and that a simple aluminium model of a star tracker is not sufficient. This also suggests that smaller star trackers are relatively close to being demisable. Unfortunately, the length scale is not sufficiently small in this case to result in demise, but it may be possible to adjust the external shape, or use holes, in order to further increase the heat flux to the surface.

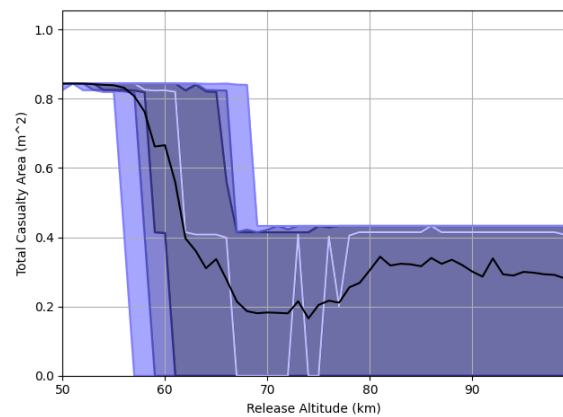
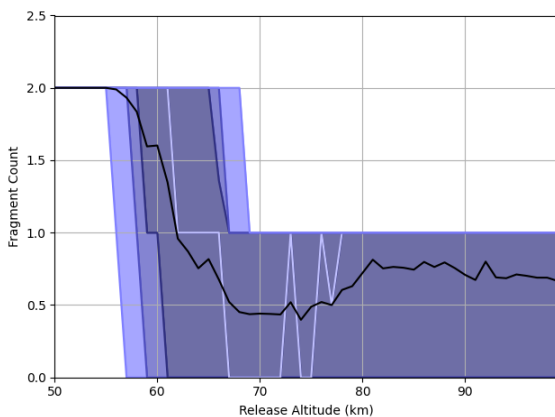


Figure 4-14: Landed Fragment Number from Small Star Tracker

Figure 4-15: Casualty Area from Small Star Tracker

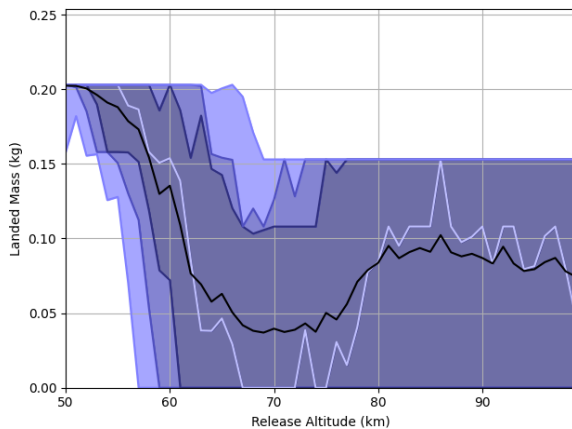


Figure 4-16: Landed Mass from Small Star Tracker

4.1.3 Modelling Conclusions

The analysis suggests that the simpler star tracker model as used in previous studies, such as PADRE, with a single titanium part, are representative of the casualty risk from a star tracker.

The performance of the model in the dynamic tests is consistent with the static tests and so no further updates to the model are required. The major lesson learned from these dynamic tests is that the titanium parts may separate, which was not foreseen in the static tests.

The current recommendation is to consider a single titanium part or a set of connected titanium parts which have no explicit separation criterion. This model will provide a single titanium landed object. Further testing of bolted joints under dynamic conditions is recommended in order to assess whether the fragmentation of parts due to the use of helicoils should be considered in simulation. These tests are not considered sufficient to recommend inclusion of this effect in casualty risk assessments at this point.

The following conclusions can be drawn regarding the modelling:

- The critical elements are the titanium parts and the shape of the barrel can create smaller length scales which increase local heating.
- The titanium demise model performs well in the test rebuilds.
- The titanium parts are joined so only one part reaches the ground. This will be the case for all relatively large star trackers, but small star trackers can have a landing probability close to 0.5.
- The PCB is also a potential risk as this is modelled in GFRP. It has to be determined whether electronics materials in equipment units should be considered as they do form a potential risk.
- This is a reduction in risk from the basic analysis due to there being only one titanium part.
- The length scale effect observed in the tests is limited for random tumbling in re-entry.

4.2 Batteries

The test samples comprise individual battery cells as well as small battery modules in different configurations provided by ABSL. Two individual cells were tested at same time in one set-up as shown in Figure 4-17. All batteries are used in the tests were passivated to 0V. The ABSL battery modules consist of 4x4 single cells, GFRP top and bottom sheets as well as nickel tags that connect the cells.

In the static test run the modules are exposed to the flow at two different angles of attack, 0° and 45°. The set-up for each angle is depicted in Figure 4-18 and Figure 4-19. In dynamic test run the module is only exposed to the flow at a 0° angle of attack.

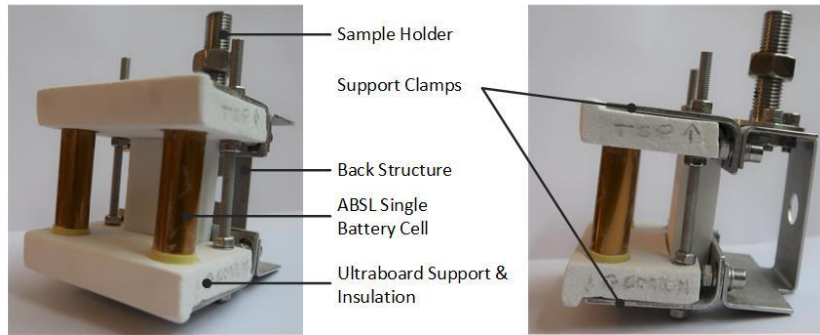


Figure 4-17: ABSL Single Battery Cell Test Sample

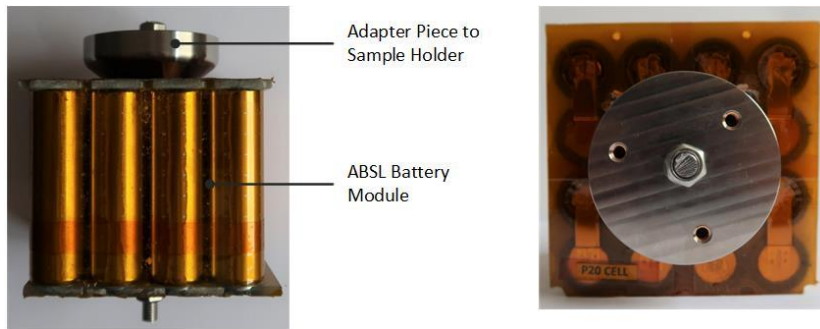


Figure 4-18: ABSL Battery Module Test Sample, 0° Angle of Attack

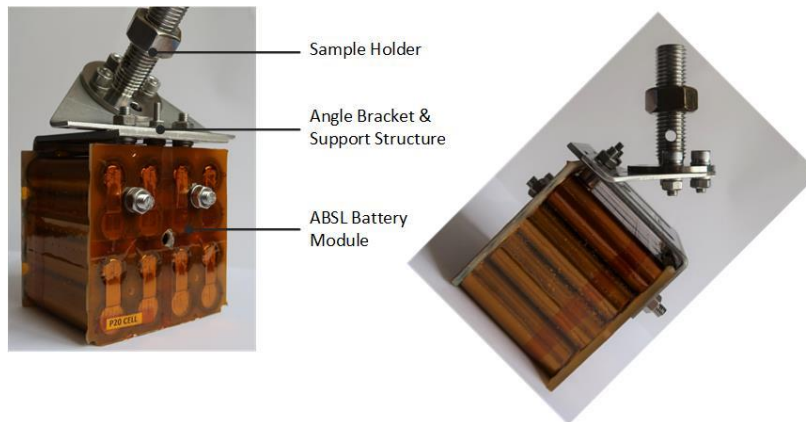


Figure 4-19: ABSL Battery Module Test Samples, 45° Angle of Attack

The first test was done with two single cell batteries. The total test duration was 452.8 s and a maximum heat flux level of 300 kW/m² was applied. After equilibrium was reached at a heat flux level of 100 kW/m², the condition was changed for a heat flux rate of 200 kW/m². The melting process slowly and steadily continued but the rate kept declining and eventually, a near-equilibrium state was reached at a heat flux rate of 200 kW/m². The heat flux was increased again to 300 kW/m² at which the sample very quickly demised.

Two battery modules were investigated. The first of these two tests had a total test time of 555 s at heat flux levels of 200, 300 and 400 kW/m². The front ledge of the GFRP sheets also melted and recessed very soon in the experiment, exposing the cap parts of the cells and destroying the thermocouples very early. However, the cells remained fixed at this stage. While the cells in the front row showed significant heating in the first part of the test, the remaining rows remained quite cool.

After the heat flux was increased to 300 kW/m², the front row cells began to demise almost instantly, starting at the outer cells first and at the inner cells about 10 s later. While the melting of the cells starting directly after the increase in heat flux, the demise process was going quite slow and, analogous to the observations in the

single cell tests, the demise rate declined as the test went on. Figure 4-20 shows the state of the samples at the end of the first phase (left), the start of demise after a few seconds at 300 kW/m² and the state of the sample just before further increasing the heat flux. The corresponding IR-images are shown in Figure 4-21.

After increasing the heat flux rate to 400 kW/m², the demise rate rapidly increases and the first row of cells is removed from the module quite fast, with the first cells taken out approximately 20 s after the increase. However, it took about another 30 s until the last cell from the first row was gone.

The cells from the second row only started to heat up significantly and consequently to demise when the cells in front of them were gone. Overall, the demise rate of the second row was slower as these cells did not heat up considerably during the first two steps of the test, as the images from the IR cameras show. It took approximately 120 s from the point, when the first cells from the front row were removed until the first cell from the second row was gone. At that point, the test was stopped.

Figure 4-22 and Figure 4-23 show images from video and IR cameras from the last phase of the test. In the left images at 435 s test time, the left two cells from the front row are removed and the cells from the second row begin to melt. At 500 s test time, the first row of cells is completely removed and the demise of the second row is in full progress (centre image). The right image shows the test at 548 s, when the first cell from the second row is removed.

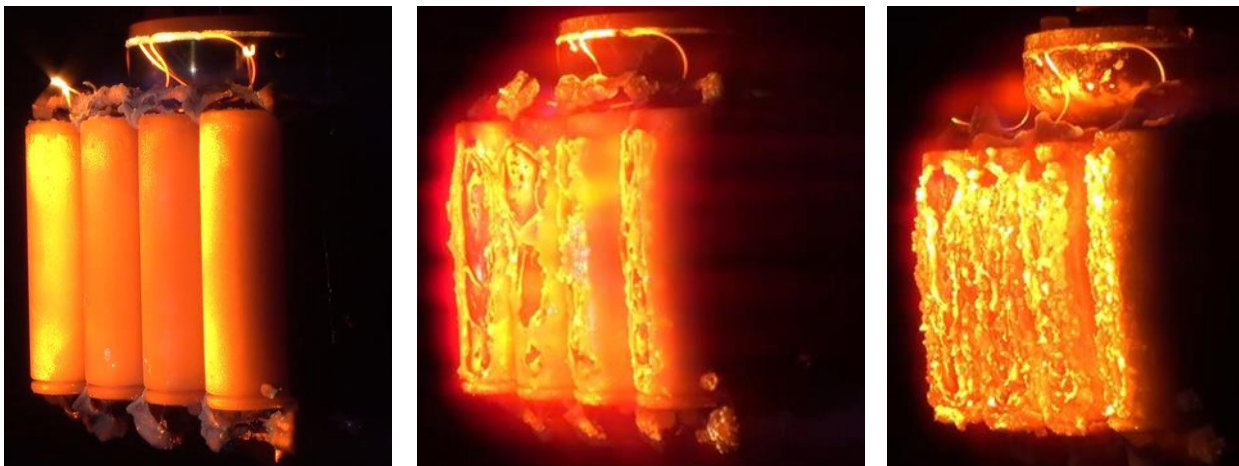


Figure 4-20: Screenshot from HD video at 180 s (left), 220 s (centre) and 400 s (right) test time

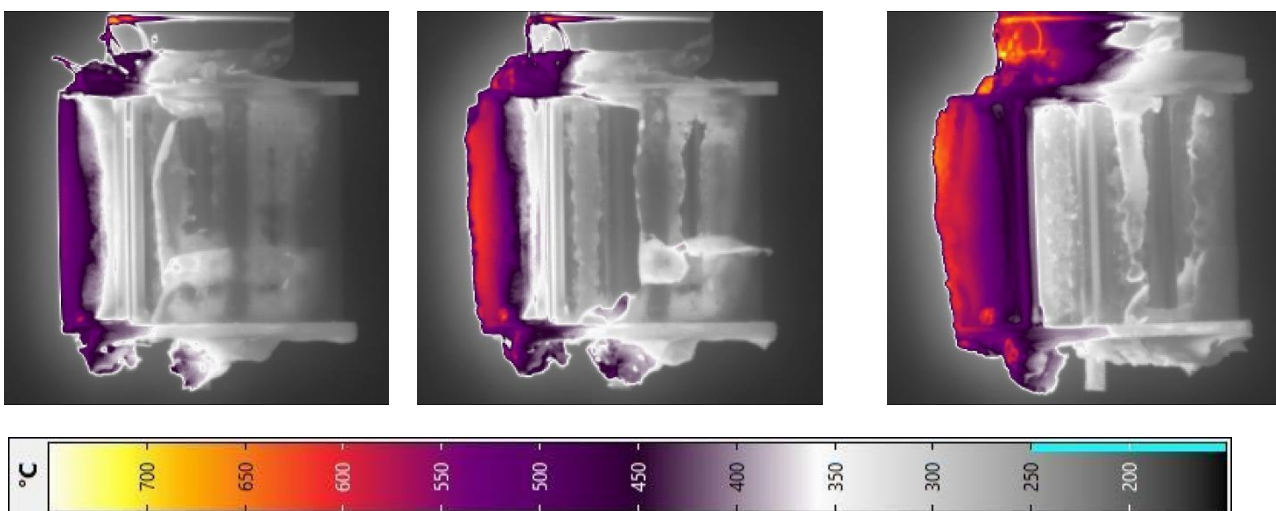


Figure 4-21: Images from InfraTec IR-camera of test S7 at 180 s (left), 220 s (centre) and 400 s (right) test time

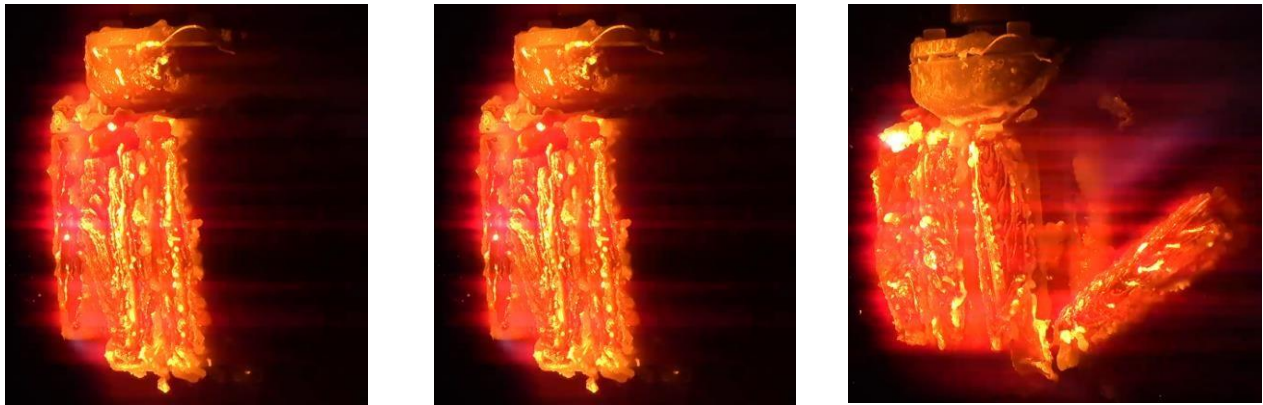


Figure 4-22: Images from HD video of test S7 at 435 s (left), 500 s (centre) and 548 s (right) test time

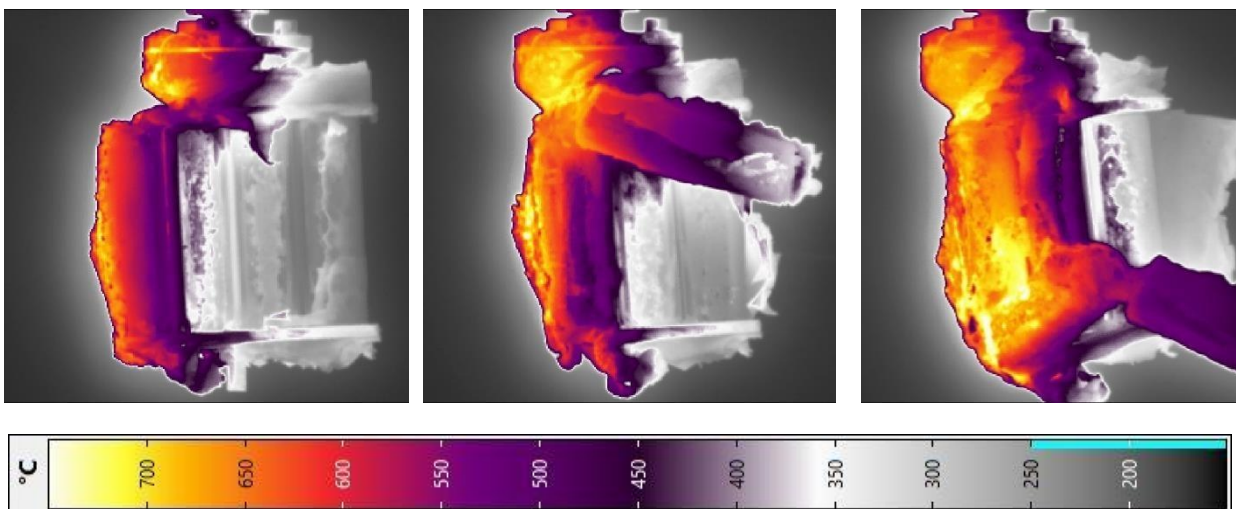


Figure 4-23: Images from InfraTec IR camera of test S7 at 435 s (left), 500 s (centre) and 548 s (right) test time

The second battery module test at an angle of attack of 45°, which has a significant impact on the sample demise. The test had a total duration of 326.0 s. The top layer of the GFRP sheet delaminated very early in the test, and the leading edge was melted and recessed so that the top caps of the cells with the metal connector parts were exposed to the flow.

Naturally, this section of the cells experienced the strongest aerothermal heating during this phase of the experiment but did not start to melt yet. This only began after the heat flux was increased to 300 kW/m². At this heat flux level, also the demise of the GFRP layer picked up and was accelerated, so that the first cells flew out of the module after about 55 s at this condition. While some melting around the top parts of the cells was observed, there was no significant demise up to this point. The cells simply could not be held anymore in the module as the GFRP sheets failed. During the next 70 s, more and more cells were removed from the module before the test was stopped shortly before the sample would have completely fallen apart.

Images from the test are shown in Figure 4-24. The left image shows the sample at the end of 200 kW/m² condition. In the centre image, the removal of the first cells from the module is shown after the GFRP layer had recessed further downstream. The final fragmentation of the sample shortly before the end of the test is displayed in the right image. The corresponding images from the InfraTec camera are reported in Figure 4-25. As observed in the previous test, only the row of cells which is exposed to the flow experiences significant aerothermal heating while the rest remains rather cold.

Overall, the demise of the sample was driven by the fragmentation due to the melting of the GFRP sheets but not the actual melting and demise of the cells and consequently, most of the cells remained quite intact. Only some cells that were strongly exposed to the flow due to the way they moved during the fragmentation process

some section with stronger melting. In contrast to this, in the case with 0° AoA the cells from the first and second rows were substantially molten before they flew out of the sample.



Figure 4-24: Images from HD-video of test S8 at 195 s (left), 260 s (centre) and 315 s (left) test time

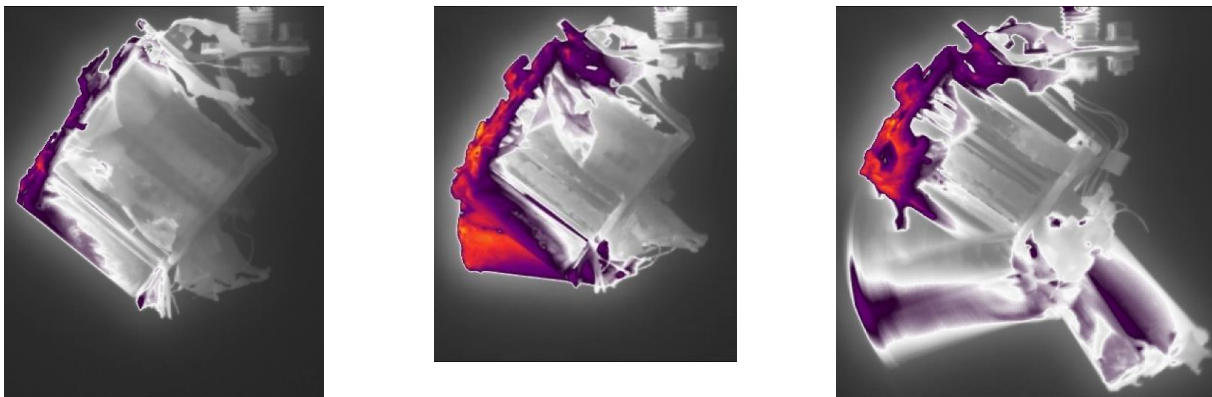


Figure 4-25: Images from InfraTec IR-camera of test S8 at 195 s (left), 260 s (centre) and 315 s (left) test time

Two battery modules were also investigated in the dynamic test set up. Both tests were started at condition with a heat flux level of 300 kW/m² and later increased to 400 kW/m². For the first test, it was further increased to 500 kW/m². The main difference between the tests was the rotation rate, 0.3 hz for the first test and 2.0 Hz for the second test.

In the static series, it was observed that for 0° angle of attack, melting of the cells was the driving factor of the demise behaviour while it was fragmentation for the case with 45° angle of attack. Here, both tests were done at 0° angle of attack, but in both cases, due to the melting of the GFRP top and bottom sheets of the modules in combination with the spinning of the samples and thus induced centrifugal forces, fragmentation was the driving mechanism in the demise. As it would be expected, the higher rotation rate and consequently higher centrifugal forces also led to much faster demise.

The GFRP sheets holding the cells start to heat up and melt/burn and recesses, especially around the corners. At the higher rotation rate of 2.0 Hz, the first cells begin to come lose after about 67 s. For 0.3 Hz, this happens after about 85 s. The cells first become lose only at the bottom and are still attached to the top layer, swinging around with the rotation of the sample for some time before being thrown off completely. As the IR images in Figure 4-26 show, the temperature distribution on the samples is very similar just before the first cells become lose, so the difference in the time when the fragmentation begins is attributed to the rotation rate and especially the centrifugal forces. As the tests continued, more and more cells became lose. First, the cells at the corners, followed by the remaining 8 outer cells. After about 125 s, only the 4 cells in the centre were left in test D08 with 2.0 Hz rotation rate. As the centrifugal forces on these cells are much lower due to the smaller distance to the rotation axis, the fragmentation was significantly slowed down. The heat flux was then increased to 400 kW/m². The heating of the cells then strongly picked up. Small holes appear in some of the cells and outgassing

of interior material is observed and it also seems like material is spilling out through the top and bottom of the cells. Also, the demise of the cover plates was accelerated. After just over 60 s at this heat flux level, remaining cells were gone and the test was stopped.

For the lower rotation rate, it took much longer for the cells to be removed. Even after they became loose at the bottom plate, they still remained attached to the top plate for a rather long time in some cases. In order to see the impact of higher heat fluxes on the demise behaviour, the heat flux was increased to 400 kW/m² after 170 s (at this point, 5 cells were left in the sample) and then to 500 kW/m² after another 104 s. Interestingly, during this phase with 400 kW/m², only one cell was removed while the four cells in the centre remained attached and saw strong aerothermal heating so that the cells started glowing and also some first signs of melt became visible. After the increase of the heat flux to 500 kW/m², the sample quickly disintegrates and the remaining cells fall off, and the test is stopped.

Images video and IR camera of the various stages of test D07 are reported in Figure 4-27. They show the sample when several cells are loose after 140 s test time but the aerothermal heating is still very low. The state after 275 s is at the end of the second phase with 400 kW/m² heat flux, just before it is further increased. At this point, all cells but the four in the centre are removed and they remaining cells have strongly heated up. Figure 4-27 then shows on the right the sample at 500 kW/m² shortly before the end of the test, when the remaining cells are being demised.

For the test at the higher rotation rate, images from video and IR recordings are given in Figure 4-28. They show the sample after 120 s test time, when several cells are thrown off by the rotation, the state after 170 s after the heat flux was increased to 400 kW/m², when only the four centre cells are left and significant aerothermal heating and outgassing and spilling of interior material is observed, and shortly before the end of the test, after 200 s, as the last cells are being demised.

For the test at the higher rotation rate, images from video and IR recordings are given in Figure 4-28. They show the sample after 120 s test time, when several cells are thrown off by the rotation, the state after 170 s after the heat flux was increased to 400 kW/m², when only the four centre cells are left and significant aerothermal heating and outgassing and spilling of interior material is observed, and shortly before the end of the test, after 200 s, as the last cells are being demised.

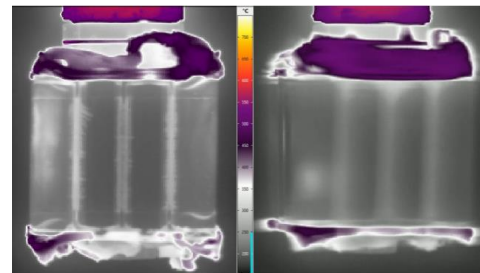


Figure 4-26: IR images of tests battery module tests with 0.3 Hz and 2.0 Hz rotation rate shortly before first cells become loose

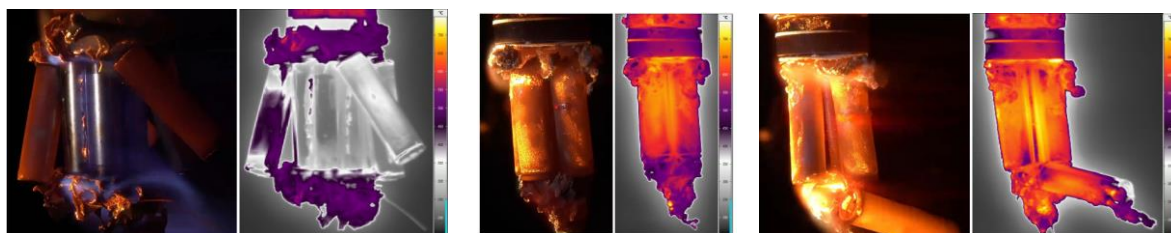


Figure 4-27: Test at 0.3 Hz - Still Frame (left) and IR (right) after 140 s, 275 s, 294 s test time



Figure 4-28: Test at 2 Hz Still Frame (left) and IR (right) after 120 s 170 s 200 s test time

4.2.1 Model Updates

From the test on the individual cells, the modified steel material appears to be suitable for capturing the cell heating and demise behaviour. This is a modification of the standard DRAMA material for steel in two ways. Firstly, the thermal conductivity is reduced by a factor of 10, and secondly the latent heat is reduced to 100000J/kg. This provides a validated equivalent material model for the cell behaviour. Although, in general, effective 'object' material models are discouraged due to the very inaccurate (and highly optimistic) legacy models for electronics and batteries, this equivalent material model has been shown to capture the cell behaviour well, and can be recommended for use. With no testing of the SAFT cells, it is assumed that their behaviour is similar. Indeed, there is no reason to suppose that the behaviour will be significantly different.

There are two other aspects of the model which require some updating. The first of these is the GFRP model. This is dependent upon work done in the modelling of the electronics cards. However, the baseline model derived in the SECRET activity performs surprisingly well for a first assessment in the rebuilds. The other aspect is more complex; this is the representation of the fragmentation of the module into cells. Different behaviour has been observed in the two module tests, with the behaviour in the angle of attack test considered to be more representative of the general heating of the block, and the normal test considered a special case. This has the advantage of allowing the heating to be modelled at the module length scale until the GFRP at the edges is removed, promoting the fragmentation. Also, once the cells have been removed, the modelling of the cells is straightforward. The difficulty comes in the fragmentation process itself.

The previous modelling effort, assessed the heating of the module as a unit to the point where the aluminium housing is considered to have failed. The attempt is then made to capture the impact of the GFRP material, and the separation of the cells into blocks. Here, the mass of the housing is retained, but inside the housing, there are four modules which are contained in GFRP. The mass of the housing has been increased to approximately one-third of the mass is housing, which is consistent with spacecraft units. Each of the modules has 500g GFRP, and releases the cells contained within based on the mass loss of the GFRP, using stochastic mass loss criterion. Note that the cells are modelled as (modified) steel, consistently with the SECRET activity findings and PADRE activity work at this stage. The critical issue here is whether the failure of the GFRP should be considered in a unitary breakup, or whether a more layer by layer failure of the cells should be considered.

Table 4-2: Battery Model with GFRP

| Component | Material | Mass (kg) | Colour | Notes |
|-----------|------------------|--------------|--------|--|
| Housing | Aluminium | 13.0 | Cyan | Contains four modules |
| Module 1 | GFRP | 0.5 | Yellow | Multiplicity used – 2 modules Contains 192 ABSL cells (each) Nested in housing |
| Module 2 | GFRP | 0.5 | Blue | Contains 48 Saft VES16 cells Nested in housing |
| Module 3 | GFRP | 0.5 | Green | Contains 6 Saft VL48E cells Nested in housing |
| Cell 1 | Steel (modified) | 0.042 (each) | Yellow | Multiplicity used (192 in each of 2 modules) Contained in Module 1 |
| Cell 2 | Steel (modified) | 0.155 (each) | Yellow | Multiplicity used (48) Contained in Module 2 |
| Cell 3 | Steel (modified) | 1.13 (each) | Yellow | Multiplicity used (6) Contained in Module 3 |

The nestedness of the model can be seen in Figure 4-29, with the modules visible in the centre image, and the internal cells visible in the right hand image. Due to the use of the multiplicity feature in the component-based model, only one of the module 1 objects requires modelling, and a single cell of each type is modelled on release. Thus, only three modules are visible in the centre image, and one cell of each type in the right hand image. The overall mass of the battery is 45kg, with 30.3kg of this the battery cells.

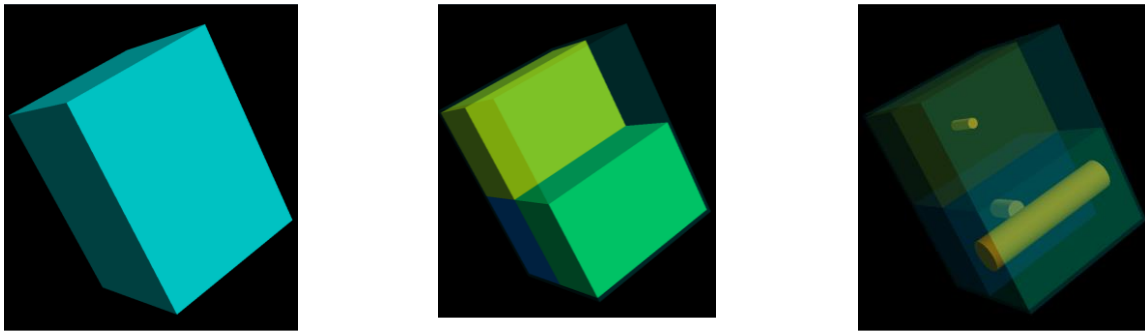


Figure 4-29: SAMj Viewer Images of Battery Model

In order to capture a layer-by-layer fragmentation, the size of the module needs to be reduced for each layer of cells removed. This is a challenge to model, and is done in stages. The purpose of this simulation is not to suggest that this is a necessary modelling approach, but to demonstrate the impact of the model as an assessment of whether a more complex model is necessary. Models for the three different cell sizes are maintained. For the large VL48 cells, there are only six cells, so there is little purpose in subfragmentation, but the other two cell types are arranged as blocks of 2 x 4 x 6 and 2 x 8 x 12 respectively. This allows the outer ring of cells to be fragmented in each case. This is shown schematically in Figure 4-30. Where the VES16 cells have two stages of fragmentation before the final separation into cells, the ABSL cells have four stages as there are more layers of cells.



Figure 4-30: Battery Fragmentation Schematic

The nested layers of the fragmentation model are shown in Figure 4-31. There is only one layer for the large cells, two layers for the medium cells, and four layers for the small cells.

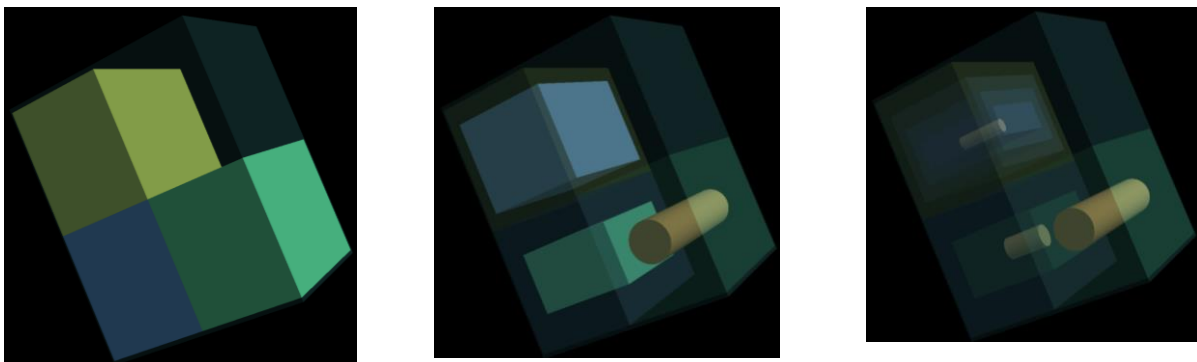


Figure 4-31: Nested Layers in Fragmentation Model

The key aspects to be considered from the dynamic set of tests are:

- Heating of the battery module appears to occur at a length scale which is smaller than the module. This would lead to increased heating of the module. However, it should be noted that this test is carried out at precisely the angle of attack for which this is most likely to occur. Where the flow impinges on the flat GFRP plates, the length scale for the heating is understood to be the module

length scale. Therefore, the heating length scale has been left unchanged. It is possible that this is a slightly conservative assumption.

- The initial detachment of the cells appears to be driven by the failure of the GFRP material. A temperature of 1200°C is suggested as appropriate based on a number of tests, inclusive of the electronics card tests, both within this activity and the SECRET activity. However, the release of the cells appears to be dependent upon the failure of the tab which joins the terminals of the cells, and this failure is dependent upon the spin rate. Based on this, the model for the GFRP failure used in the previous analysis is considered sufficient.

The large battery modelled is considered to represent only a particular class of very large battery. Therefore, in addition to this, a range of battery sizes, from 10kg to 30kg, are considered. To assess the different sizes of battery, three batteries are considered, each considering the standard, tested, ABSL cells. The units considered are given in Table 4-3.

Table 4-3: Updated Battery Models

| Battery | Component | Material | Mass (kg) | Notes |
|---------|-----------|------------------|--------------|----------------------------|
| 10.22kg | Housing | Aluminium | 3.0 | Contains two modules |
| | Module | GFRP | 0.25 | Contains 80 cells (10x8) |
| | Cells | Steel (modified) | 0.042 (each) | |
| 20.44kg | Housing | Aluminium | 6.0 | Contains four modules |
| | Module | GFRP | 0.25 | Contains 80 cells (10x8) |
| | Cells | Steel (modified) | 0.042 (each) | |
| 30.66kg | Housing | Aluminium | 9.0 | Contains four modules |
| | Module | GFRP | 0.375 | Contains 120 cells (12x10) |
| | Cells | Steel (modified) | 0.042 (each) | |

The GFRP model used is that derived from the electronics cards tests. The module layout is shown for the largest battery in Figure 4-32.

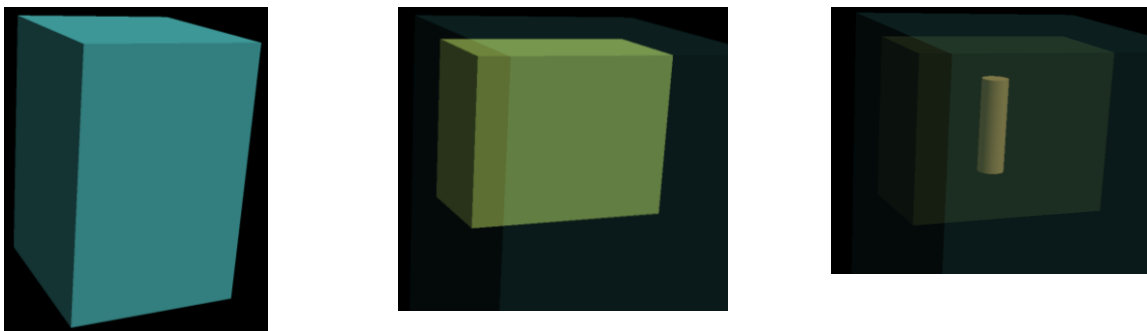


Figure 4-32: Updated Battery Model

Additionally, the GFRP material is considered to have been split into small parts during the fragmentation of the modules and so is not considered to pose a risk at the ground in these analyses. The release of the cells is maintained as occurring at a point when a mass of the GFRP has demised, and this is maintained as a uniform distribution between 0.3 and 0.7. It is possible that this could be slightly conservative.

These models were run using the same initial conditions and uncertainties as the previous battery models.

4.2.2 Re-Entry Simulations

The two updated models are run using PADRE the uncertainties in 4.1.2. Note that the battery mass is large, at 45kg. Most spacecraft batteries will be smaller than this, so it is quite an extreme case.

Relative to the star tracker, the PADRE analysis is more complex as a very large number of parts can land when the battery is released late, due to the possibility that the cells are released, but do not demise. This is a possibility for the ABSL cells for release altitudes below 70km, and for the VES16 cells at release altitudes below 78km. The predicted number of landed objects shown in Figure 4-33 demonstrates the potentially large risk from the cells. The detail of when the cells demise is also difficult to see on this figure. This is best understood by use of the median (white) line. At high altitudes, the casualty risk is very small, with about a 15% probability of the VL48E cells reaching the ground, so the median risk is essentially zero. It is interesting to note that, although the GFRP releases the cells in all cases above 70km release altitude, the model allows the remaining GFRP to be propagated, and the large mass of GFRP is not completely demised in a significant number of cases. This is not a realistic scenario, and requires fixing in the model for the next iteration. The VL48E cell lands in the median case at about 76km release altitude, and there is a very small probability of the VES16 cell landing above 80km.

Between 70km and 80km, the landed object count remains small as the probability of the VL48E cells surviving reaches 69%, but the VES16 cells are at about 5% and the ABSL cells at 0.2%. The VES16 cells land in the median case once the release altitude reduces below 66km. The ABSL cells land in the median case at 62km. It is noticeable that for release altitudes below 54km, the median drops, which suggests that the cells are not released at these low release altitudes as the housing / module GFRP does not demise sufficiently to release the cells.

The landed mass provides a consistent picture as shown in Figure 4-34. The median (white line) is close to zero until about 76km, once the VL48E cells land in the median case. This increases monotonically until the majority of the battery survives as a complete object, with the housing partially demised, at 50km release altitude.

It is clear from this work that there are two aspects of this model which require an update. The first is the landing of GFRP parts which will be disintegrated during the fragmentation into cells, and the second is that a smaller battery, with total mass 30kg should be considered. The updated GFRP model from the electronics work will also be considered. This will be done after the second test campaign.

Although this is the case, a comparison of these results with the assessment of the layer-by-layer fragmentation model can be made. The landed fragment count is shown in Figure 4-35, and suggests that the critical release altitudes for objects reaching the ground are significantly lower, which is positive for demise, but the potential number of objects which can reach the ground is significantly higher. This suggests that it is very important to ensure that the battery is released at reasonably high (>70km) altitude to ensure demise occurs.

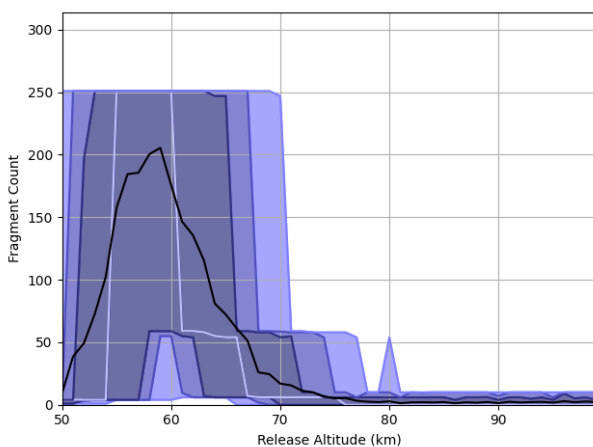


Figure 4-33: Landed Object Number from Baseline Battery Model

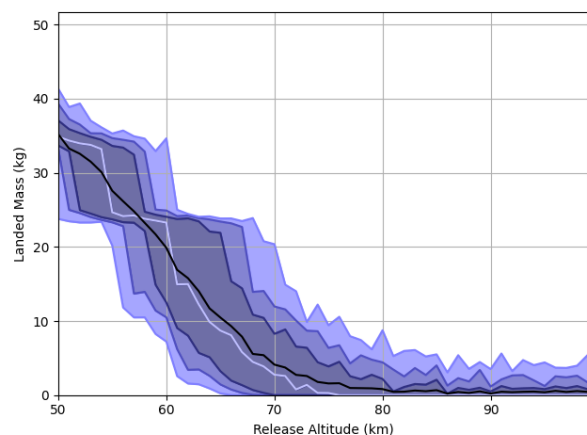


Figure 4-34: Landed Mass from Baseline Battery Model

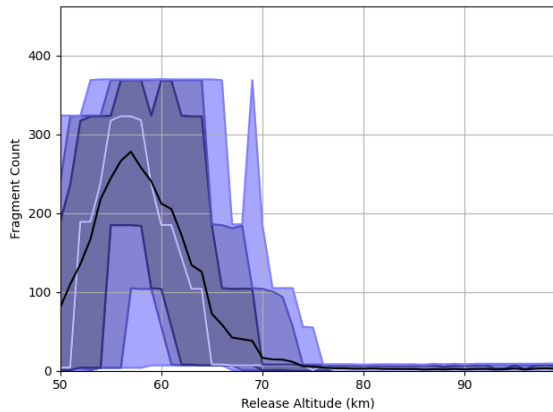


Figure 4-35: Landed Fragments from Layer-by-layer Battery Fragmentation

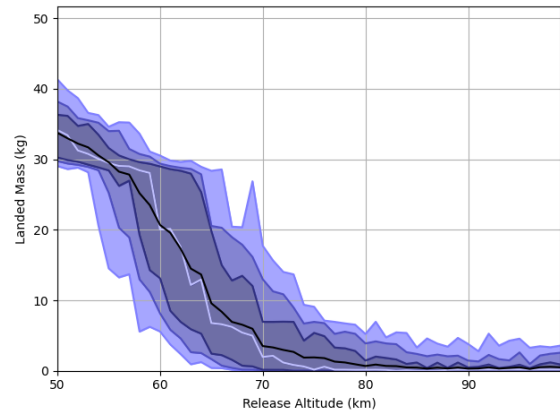


Figure 4-36: Landed Mass from Battery Fragmenting Layer-by-Layer

Once again, there is some signal from partially demised GFRP parts which is not realistic and needs to be fixed in the next version of the model. The behaviour of the large VL48E cells is essentially the same as the layer-by-layer fragmentation is not applied to them as they are small in number. The probability of the VES16 cells reaching the ground is reduced between 70km and 80km to about 3%, but the probability of the ABSL central cells reaching the ground is slightly higher. The central ABSL cells and the VES16 cells are expected to reach the ground in the median case from release altitudes under 64km, which is slightly higher than the median value for the ABSL cell block when fragmented all at once. This is reasonable, as it takes longer to reach the interior of the block. More cells are predicted to be released at the lower altitudes as the fragmentation proceeds layer-by-layer, which is certainly more realistic, and there is a much lower probability of the modules remaining intact and the cells not being released. The steps in the median line between 76km and 58km release altitude show each layer of the ABSL cells landing in the median case.

The landed mass shows a very similar trend to the baseline model, as shown in Figure 4-36, which suggests that the layer-by-layer fragmentation does not have a major effect. A deeper investigation of the numbers suggests that the landed mass is about 10% lower than for the baseline model for release altitudes between 60km and 80km, so the impact is measurable, but not large. There is a small benefit from using this approach, but a significant risk as the worst case scenario is significantly worse.

This suggests that the complexity of the layer-by-layer model does not make a significant difference in a stochastic sense, and it is suggested that this approach is not investigated further.

Overall, the results suggest that a 45kg battery with ABSL cells is fully demisable from a release altitude of 70km, and a similar battery containing VES16 cells is fully demisable from a release altitude of 75km. These values are significantly above the median values, as there are a large number of objects released, and for the mean number of objects to be small, the critical release altitude much be such that the probability of the objects landing is very low.

Starting with the large 45kg battery which was used in the analysis after the first test campaign, the use of the updated GFRP model can be seen to have a slightly negative impact on the results, suggesting that the updates have made the GFRP slightly less demisable. As visible in Figure 4-37, the VL48 cells are now marginal on demise from very high altitude, and consistently land in the median case from about 85km. The story is less critical for the smaller cells, with the VES16 cell now landing in the median case when released from 68km (was 66km), and the ABSL cells at 62km, which is the same as in the previous analysis.

In the previous analysis (Figure 4-33) there is a region between 54km and 62km where the cells are released and do not demise, resulting in a high casualty risk. In this case, as the GFRP is less demisable, the cells are not fully separated if the battery is not released below 58km, resulting in a reduced risk below this release altitude.

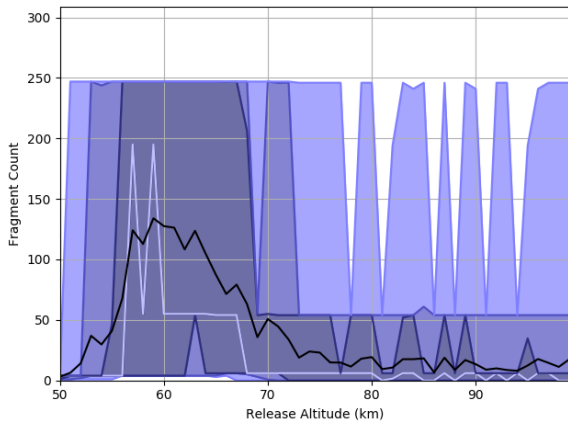


Figure 4-37: Fragment Count from Updated Battery Model Simulation

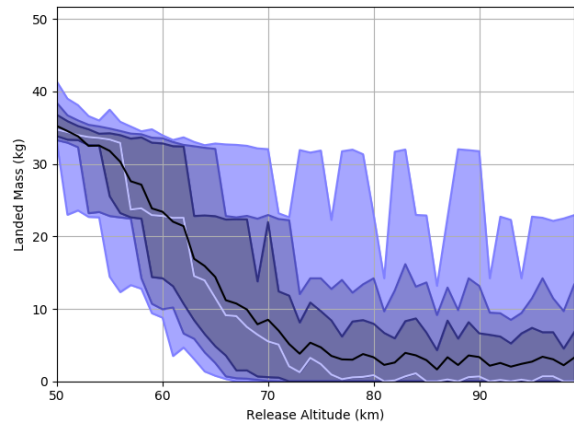


Figure 4-38: Landed Mass from Updated Battery Model Simulation

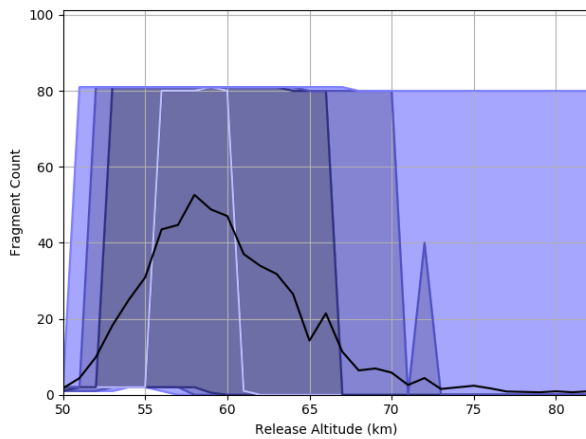


Figure 4-39: Fragment Count from 10kg Battery Model Simulation

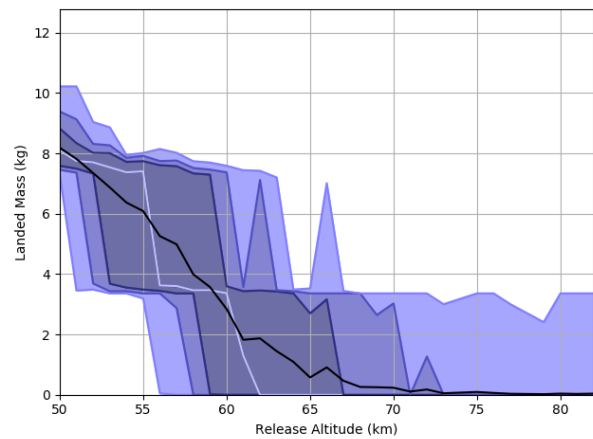


Figure 4-40: Landed Mass from 10kg Battery Model Simulation

The slight increase in the GFRP demise resistance is also evident when comparing the new landed mass results in Figure 4-38 with the old results in Figure 4-34. The new landed masses are higher throughout, and have a larger variability.

Applying this model to a 10kg battery, which is constructed with ABSL cells only, the results of Figure 4-39 are obtained. In this case, there is no risk predicted by SAMj/PADRE for any release above 82km, with the median risk of the cells reaching the ground with risk altitudes below 62km. Interestingly, there is a small residual risk as there is a probability that the cells can reach the ground from 82km, but this contributes a mean casualty area of less than 0.5m².

This is consistent with the landed mass shown in Figure 4-40. The mean mass landed is very small up to the point that the battery is released from the spacecraft below 65km. As this is considered a very late release, the 10kg battery poses a very small ground risk.

For the 20kg battery, the story is very similar. The altitude at which there is some risk of the battery cells reaching the ground rises from 82km to 88km as shown in Figure 4-41. However, the median case where the battery cells land increases only to 63km. There is a higher risk from this battery, as should be anticipated given its larger mass, but it is not substantial, and again the expected casualty risk from a standard uncontrolled re-entry from a decaying circular orbit is small.

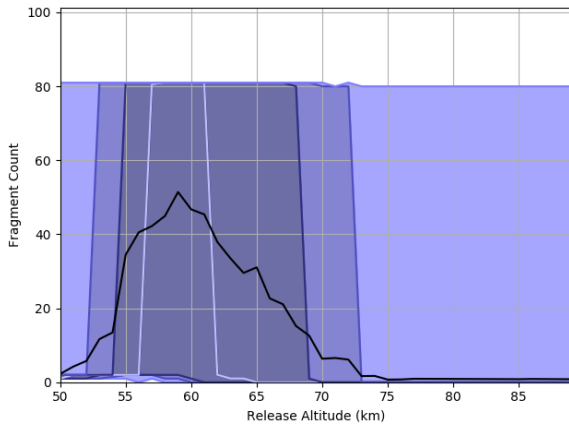


Figure 4-41: Fragment Count from 20kg Battery Model Simulation

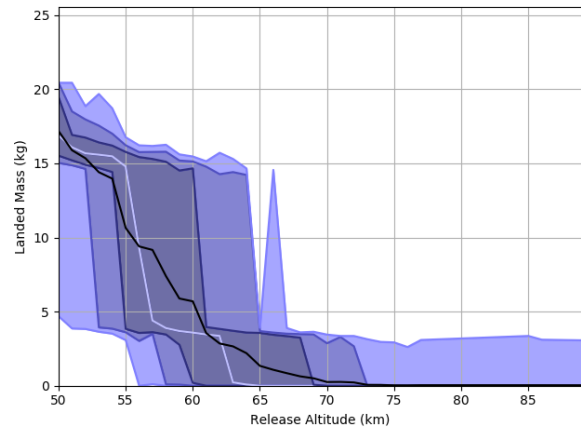


Figure 4-42: Landed Mass from 20kg Battery Model Simulation

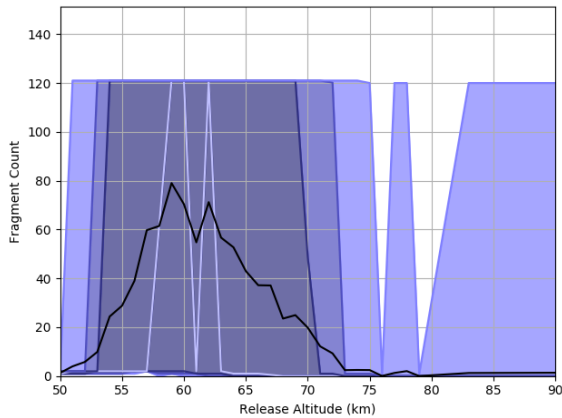


Figure 4-43: Fragment Count from 30kg Battery Model Simulation

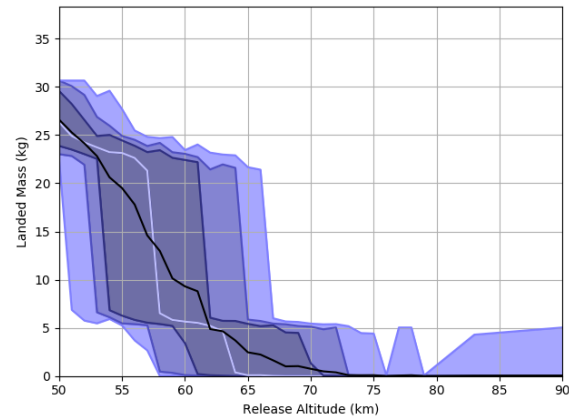


Figure 4-44: Landed Mass from 30kg Battery Model Simulation

The final case analysed is the 30kg battery. In this case Figure 4-43 and Figure 4-44 shown that the battery cells can land from release altitudes up to 90km, but that there is a very low probability of landing until the release altitude reaches about 72km. The cells land in the median case at 63km. This further demonstrates that batteries are a low casualty risk object when small cells are considered. It is important to note that the use of larger cells increases the casualty risks, and more data is required on the demise of larger cells.

4.2.3 Modelling Conclusions

Two parts of the current model are not available in DRAMA. The first is the ability to model GFRP using the balance integral approach of the SAMj model which was demonstrated within the COPPER activity, and the second is the use of a mass loss criterion to initiate fragmentation. It is worth noting that both of these capabilities are being considered for addition to DRAMA in the near future.

Without these modelling capabilities, the missing behaviour of the model is in the representation of the fragmentation of the battery. In order to assess this, the 30kg battery has been run using the equivalent metal GFRP model and no specific fragmentation criterion. The landed fragment number is shown in Figure 4-45 and the landed mass in Figure 4-46. In comparison with Figure 4-43 and Figure 4-44, it is evident that the maximum release altitude at which survival is possible decreases significantly. This difference is due to a small number of outliers in the more sophisticated model, which do not significantly affect the overall statistics. Indeed, the statistical behaviour is reasonably similar, with a very similar release altitude range for which the cells are released and are able to hit the ground. Indeed, this model supports the assertion that, for cells of this size, batteries up to 30kg can be considered a low casualty risk.

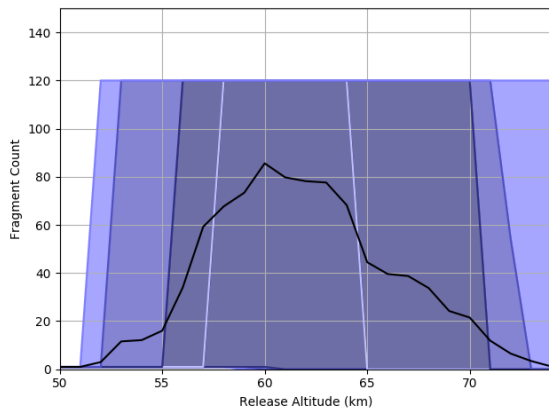


Figure 4-45: Fragment Count from 30kg Equivalent Battery Model Simulation

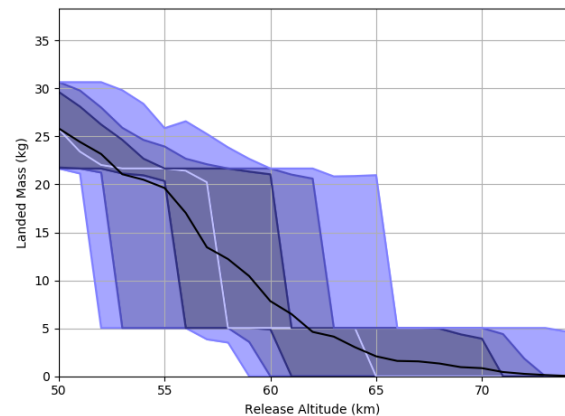


Figure 4-46: Landed Mass from 30kg Equivalent Battery Model Simulation

The simplified equivalent GFRP model is slightly optimistic, but sufficient for use in DRAMA for battery module demise, particularly for smaller batteries as these are not expected to be critical objects.

The following conclusions can be drawn regarding the modelling:

- The steel model proposed in SECRET is confirmed as suitable for the ABSL batteries tested, and these tests suggests that the latent heat can be reduced in the model, slightly increasing demisability.
- Fragmentation is driven by the GFRP failure in the angle-of-attack test, which is considered more representative for flight.
- The modelling of the GFRP modules has an impact on the demisability, but not sufficiently to change the prediction of demise for small cells.
- Batteries with small cells are expected to demise completely from most release altitudes of interest.
- The current model has remnant of GFRP landing and causing a risk. This requires correction after the second test campaign.
- A more complex layer-by-layer approach was attempted, and created a small increase in demisability. The added complexity is not considered to be worth the change statistically.
- Larger cells show lower demisability. The small Saft cells are predicted to demise, but the larger Saft cells will pose a risk when using a steel material model.
- The potential risk from batteries is very large as there is the potential to land a large number of cells. The median case is not a reasonable assessment in this case.
- The use of an equivalent metal model is slightly optimistic, but is considered suitable for use in statistical DRAMA analyses.

4.3 Electronic Equipment

The test samples comprise different types of PCB used in different electronics applications:

- PCDU Board
- Battery Control Board (BCM)
- Power Distribution Board
- Unpopulated EnMap PCB

The boards were cut into smaller section to comply with sample size envelope of 100 mm x 100 mm. Each PCB sample can be mounted at two different angles of attack, 0° and 45° as shown in examples in Figure 4-47 and Figure 4-48.

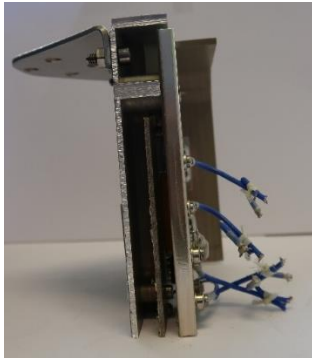


Figure 4-47: PCB, 0° Angle of Attack

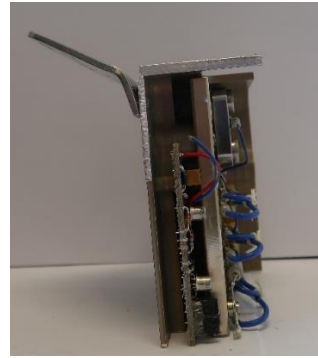


Figure 4-48: PCB, 45° Angle of Attack

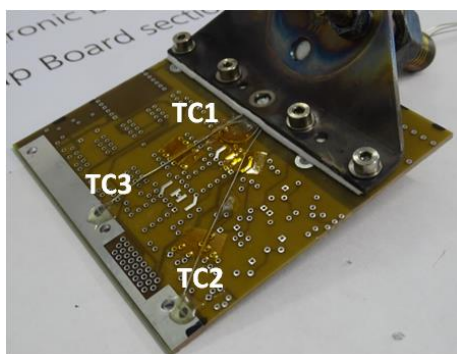


Figure 4-49: Enmap PCB Sample

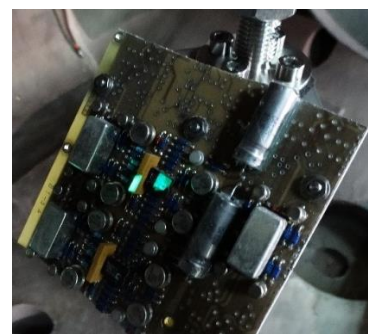


Figure 4-50: PD Board Sample

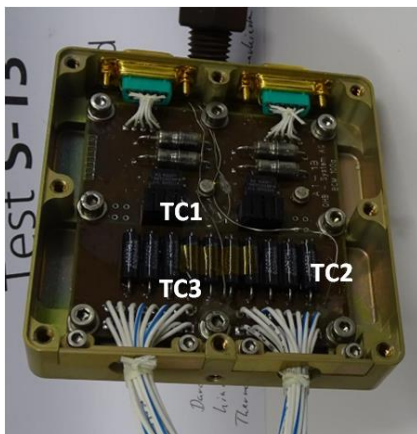


Figure 4-51: BCM Sample



Figure 4-52: PCDU Board Sample

The static test with the unpopulated EnMap board was conducted to assess the impact of a higher heat flux, i.e. the test was started directly with a heat flux of 300 kW/m². The test lasted for just over three minutes (180.9 s). The top layers of the GFRP board of the sample started to delaminate right at the beginning of the test from the leading edge, driven by the shear stress of the on-coming flow, and the sample was bent backwards around the sample holder. At the bend which then constitutes the stagnation point of the sample, the EnMap board then begins to melt. This happens in the first 25 s of the test.

During the further course of the test, the sample keeps on melting around the stagnation area until it is almost completely recessed. This process takes quite a long time, approximately 155 s, before the test is stopped. Images from the beginning of the test exposing the delamination of the top layers of the sample leading edge and the bending of the sample around the sample holder are displayed in Figure 4-53. The melting of the sample around its stagnation area in the middle of the test and the state just before the end of the test are also.



Figure 4-53: Delamination of GFRP layers at the leading after 5 s (left) and bending of the board around the sample holder after 25 s; Melting of EnMap board at the middle and just before the of the test (right)

A section of a PD board was investigated in a static test. For this test, a stepped approach was chosen, starting at the lowest heat flux level of 100 kW/m². It is interesting to note that in contrast to the unpopulated board, the PD board section does not delaminate around the leading edge at the start of the experiment. If this is due to the lower heat flux and also lower pressure associated with this condition, cannot be concluded. On the other hand, several of the components, especially those close to the leading edge, strongly heat up and are removed from the top of the board early in the test, i.e. in the first 60 s.

It also took comparably long for the PD board section to be bent back around the sample holder. This only started after about 80 s test time and the process was quite slow, as it took about 30 s for the sample to reach a rather steady position again. It is interesting to note that during the bending, the coating on the bottom side detached from the surface. Naturally, the bending of the sample around the holder caused strong heating around the new stagnation area and especially of the electronic components in this area but this did not cause the further removal of some of these parts.

As the test went on, the sample continued to gradually bend further backward up to about 270 s test time, where it reached another steady state and also thermal equilibrium. After a further 30 s at this condition, the heat flux was increased to 200 kW/m². The GFRP of the PD board now started to melt around the stagnation area which also caused the removal of further components from the board. The melting process around the stagnation area continued steadily. After more than 190 s at this heat flux level, it was decided to further increase to the heat flux in order to achieve the complete demise of the sample. After the higher heat flux of 300 kW/m² was reached, the melting rate of the sample increased and quite soon, after approximately 10 s, the first holes in the sample can be observed. About 15 s later, the main part of the board actually detaches from the section mounted to the sample holder, but it gets stuck at the screws in the substructure of the holder, so it does not fall down but continues to demise. The test goes on for almost 30 s more before it is stopped.

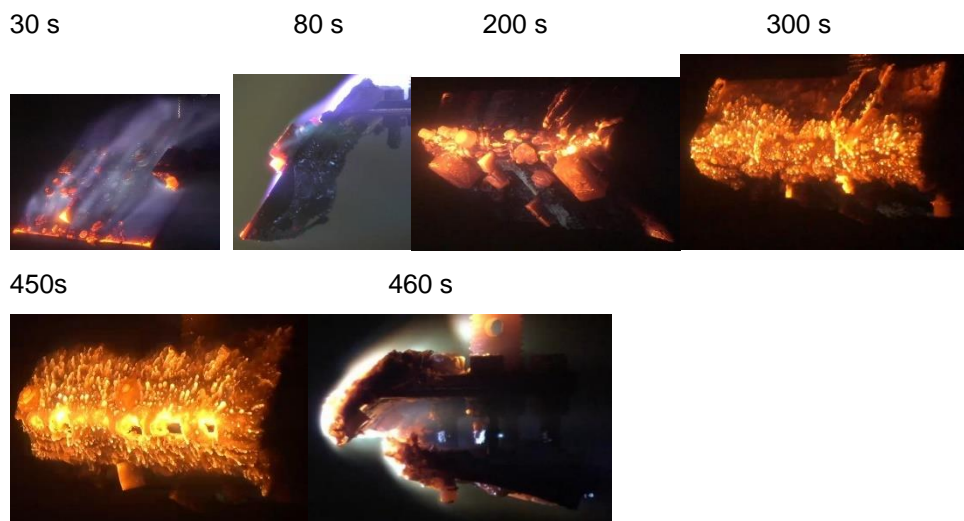


Figure 4-54: Sequence of images from PD Test

A sequence of images illustrating the course of the test is presented in Figure 4-54: The heating and removal of components without delamination of the board after 30 s, the stripping of the coating on the bottom side at

80 s, the heating of the stagnation region at 200 s and the melting in this area after 300 s, and finally, the development of holes in the board and the detachment of the board close to the end of the test.

In the test with PCDU board section, not only the board itself but also a considerable part of the aluminium housing was investigated. The test lasted for 259.9 s in total. The impact of the housing on the sequence of the test was not very significant. While it protected the leading edge of the board from the on-coming flow, still many of the board components heated up strongly and were removed early in the test. The housing itself also melted and parts also flew away very early in the test, and the bending of the sample around the holder was only slightly delayed. However, as the previous tests had different initial conditions, this is difficult to compare. At a test time of 45 s, the housing was either gone or wrapped behind the back of the sample, which itself was already bent quite far back around the holder so that the state was similar to the previous tests. As before, melting of the board and strong heating of the board components around the stagnation region dominated the rest of the test. The sample was also bent further back around the holder (from 60 s test time to 140 s). To accelerate the demise process, the heat flux was increased to 300 kW/m² after almost three minutes test duration. Consequently, the melting rate increased and after a little less than 80 s at this condition, the test was stopped shortly before the sample presumably would have failed.

The test sequence is illustrated by the images in Figure 4-55. These images show the state when the aluminium housing is melting and some components are removed from the sample at 35 s test time, and 10 s later, the housing is already gone and the sample bent back quite far. The image at 170 s shows the state before increasing the heat flux to 300 kW/m² and the last image at 260 s just before the end of the test.



Figure 4-55: Test S14 at test times of 35 s, 45 s, 170 s and 260 s

Two tests were conducted with the BCM samples. The first one was done with the single BCM board where the board was coated but without the lid of the housing. The test lasted for 332.1 s and was started at 200 kW/m² and later increased to 300 kW/m². The cables hanging from the sample melted very quickly, i.e. in the first 30 s of the test. The frame of the housing around the board is heated up very fast as well and most of it demises within the first 60 s. As in the previous tests, the sample is consequently bent around the sample holder. The part of the housing underneath the board, however, remains attached to the board. This however, does not appear to have a considerable impact on the demise behaviour. Instead, the further course of the test is analogous to the previous tests, i.e. there is strong heating and melting of the sample in the stagnation area where the sample is bent around the holder. After reaching a steady state, the heat flux was increased to 300 kW/m². This led to the lower part of the sample detaching from the rest after only 5 s and the test was stopped.



Figure 4-56: Test S13 after 60 s test time (left image), 90 s and 300 s

Figure 4-56 presents a sequence of images from the test. The first picture shows the sideview after 60 s and visualizes the melting of the frame of the housing and the starting of the bending of the sample. After 90 s,

displayed in the top right image, the sample is bent all the way backwards and the heating/melting of the stagnation are begins. The bottom right picture shows the state at 300 s before the heat flux was increased.

In the second test, two BCM boards had been stacked together on top. In this case, the top BCM also had the lid of the aluminium housing mounted on top. The test lasted for 241.8 s at 200 kW/m². The heat flux was not increased during the test. As in the test with the single BCM, the cables melt very fast at the beginning of the test. The housing begins to melt after about 35 s, starting from the outlet holes of the cables and slowly propagating upstream the lid first and then towards the sidewalls of the frame. This melting process delays the overall demise process of the board. Due to the stabilization from the second board underneath, the sample does not bend around the sample holder in the early phase of the test. Instead, the top surface of the upper BCM strongly heats up and also starts melting from the leading edge. The components on the board are blown away. As the frame of the housing is already gone at this stage, there is no fixed connection in between the two BCMs. The top one simply stays in place as it is pushed onto the bottom one by the oncoming flow.

After 120 s test time, the upper board suddenly bursts into several pieces which are consequently blown away (see Figure 4-57 and Figure 4-58). Over the remaining test time, the behaviour of the lower board then is analogous to test S13 with the single BCM. The board strongly heats up and is bent around the sample holder and the starts to melt around the stagnation area. After just over four minutes test time, the test was stopped. At this point, the state of the remaining sample was very similar to the first test before the heat flux was increased. Consequently, it was also expected that the sample would have failed very quickly if the heat flux had been increased in this test as well. Images to illustrate the different phases of the test are displayed in Figure 4-57 and Figure 4-58.



Figure 4-57: Stacked BCM Test at test times of 60s, 100 s, 120 s

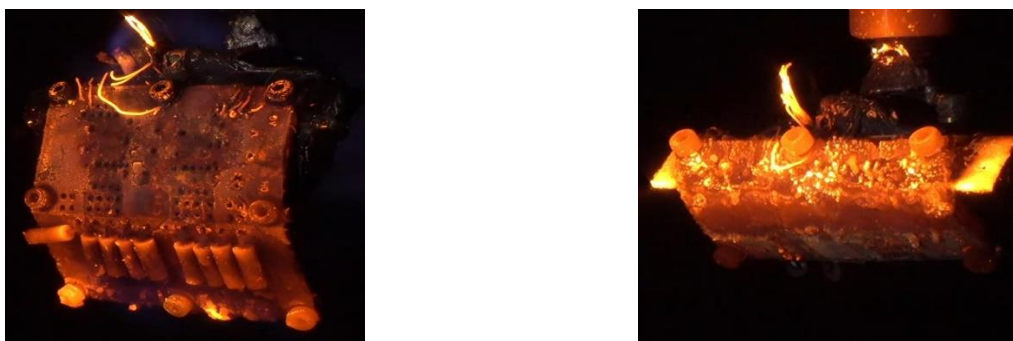


Figure 4-58: Stacked BCM Test at test times of 135 s and 240 s

The two more static tests were performed with the unpopulated EnMAP board and the PD board. They were both started at a low heat flux level of 100 kW/m² which was later increased to 200 and 300 kW/m². In the first stage of the tests, the coating of the boards burns away. It takes approximately 60 s for the EnMap board and 70 s for the PD board for the coating to be completely removed (visible by the disappearing of the outgassing of material). In the latter case, this is also influenced by the heating and removal of some of the components on the board as well as the cables and connectors. The samples further heat up at this condition, and a few additional parts are removed from the PD board but apart from this, no notable events occurred. After approximately 3 minutes test time for the EnMap board and 4.5 minutes for the PD board, the heat flux was increased to 200 kW/m².

Subsequently, the board material begins to melt and is carried away by the flow over the edges of the samples. The melting and erosion rates are quite low, however. For the PD board, substantial parts of the board surface are covered by various pieces and thus the melting rate is even slower as only exposed sections are melted. The heating rate of the components on the PD board is also slightly increased and some further parts are removed by the flow, but it remained at a slow rate and the board with its components stayed quite intact until the heat flux was further increased to 300 kW/m².

This was done after almost 8 minutes test time for the PD board and approximately 6 minutes for the EnMap board. At this condition, the demise rate strongly picked up. The melting of the board material was strongly increased. On the PD board, the remaining component were demised and either completely melted or were otherwise removed within 30 s after increasing the heat flux level. After that, the melting of the board material continued.

It is difficult to tell when the first holes in the board material appear. For the EnMap board, it looks like after about 7 min test time, the first locations where the board was completely molten appear close to the right edge. After about 8 min test time, the line of a thermocouple becomes visible in the lower left section of the board. After that, the amount of molten material that is pushed towards the edges of the sample gradually declines, suggesting that the more and more of the board surface is fully demised. The test is then stopped after 9:40 min test time. On the PD board, it is more difficult to recognize spots where all the board material was removed. The rate at which molten material flows to the edges of the sample starts to decline after about 10:30 min test time. The test is stopped after just over 13 min test duration.

Although the time points of increasing the heat flux are rather randomly chosen, it is notable that the populated PD board takes much longer to demise. The time at each heat flux step was significantly higher than for the EnMap board. It is assumed that this is simply due to the fact that the demise of the components on the board also requires a certain energy intake, and that as long as they are not removed, they also shield the basic board material from the exposition to the flow. For the EnMap board, on the other hand, the heating and demise of the board starts directly at the beginning of the test.

Images from both tests at the end of the first two heat flux steps as well as during full demise of the sample before holes in the material appear, are shown in Figure 4-59. Post-test photographs of the samples are displayed in Figure 4-60.

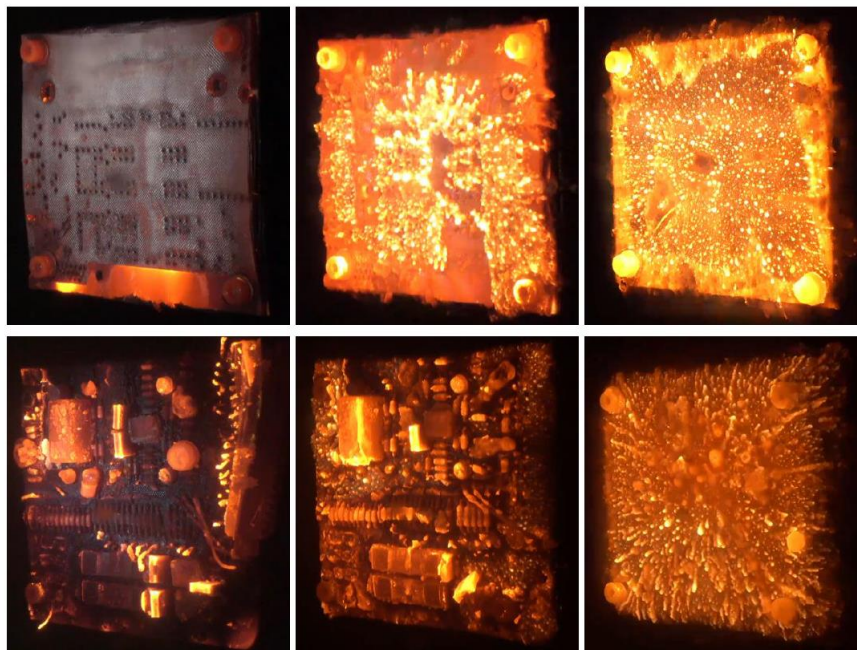


Figure 4-59: EnMap (top) and PD (bottom) board sections at the end of 100 kW/m² (left) and 200 kW/m² (centre) heat flux steps and during full demise at 300 kW/m² (right)

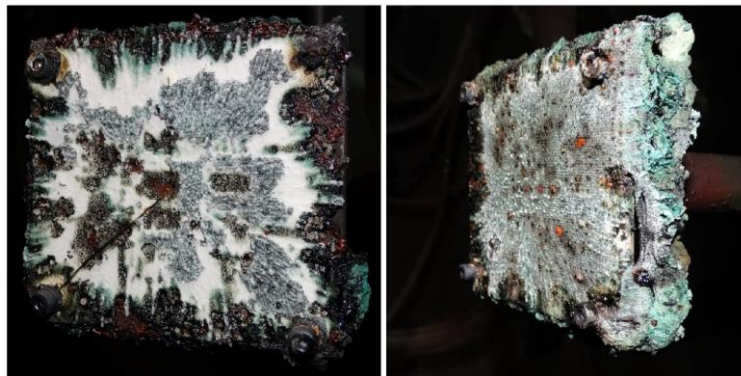


Figure 4-60: EnMap (left) and PD (right) board sections after the tests, still mounted in L2K

In the dynamic set up the EnMap and PD boards were tested at rather low rotation rates of 0.5 and 0.1 Hz, respectively. The heating of the sample reduced the stability of the base material of the boards which consequently were bent around the sample holder. This gradually increased until the samples were flapping back and forth because of the rotation and the oncoming flow. In the case of the EnMap board, it can be observed that the matrix of the GFRP material apparently cracks at a point approximately one third of the sample height from the top early in the test (after about 15 s). Although most likely the fixation of the samples would have failed at some point if the heat flux rate was kept at 200 kW/m², it was increased to 300 kW/m² after 64 s test time for the EnMap board and 108.7 s for the PD board, in order to see the effect of the increased heat flux. As expected, this accelerated the demise rate of the sample especially in the part that is fixed to the holder. It also caused the faster demise and removal of remaining components on the PD board, which, similar to the stagnation test, were not much demised at the lower heat flux level.

The bending of the samples around the model holder and thus induced load changes also become notably stronger. This is not only due to the increased heating of the GFRP material and consequent further loss in stability, but also due to the increased Pitot pressure at the higher heat flux condition. The tests were finished after the board material failed close to the holder and the major parts of the boards flew away. This happened after 69.8 s for the EnMap board and 57.2 s for the PD board at the 300 kW/m² condition. In the case of the PD board, the main part was thrown into the diffusor of L2K and could not be retrieved.

Images from the video cameras of test with the EnMap board section are shown in Figure 4-61. These show the crack in the sample after 15 s test time (left image), the state just before increasing the heat flux with the sample strongly bent around the sample holder (centre image) and the sample nearly demised shortly before the test is stopped (right image). For test with the PD board images in Figure 4-62, after 60 s test time (left image), just before the increase to 300 kW/m² (centre image) and shortly before the sample breaks off (right image).



Figure 4-61: Images from video cameras of EnMap board test after 15 s (left), 64 s (centre) and 130 s (right) test time



Figure 4-62: Images from video cameras of PD board test after 60 s (left), 108 s (centre) and 172 s (right) test time

Although the basic sequence in the tests is very similar, there are also differences, for example, the test times are quite different. As there are two major differences between the tests, the components on the PD board and the rotation rate, it is difficult to conclude what the definite causes are for these differences, but some possible explanations can be made from observations in the tests. In the stagnation tests we have already seen that the PD board with multiple components takes longer to demise as these components also require a certain energy intake to demise and/or be removed, and also shield the basic material, and possible also enhance the stability of the board. The lack of these component might have played a role in the cracking of the EnMap board soon after the start of the test.

The rotation rate has several impacts. For once, it directly determines the number of load changes that the sample experiences and also the magnitude of the centrifugal forces. Furthermore, during each rotation, each side of the sample sees a heating face when it is facing the flow and a cooling phase when it is directed away from the flow. This is especially important for the area fixed to the holder. While the total heating and cooling time in a given period are independent of the rotation rate, the transient character of these processes can have an impact on the total heating.

The dynamic test of the full BCM was only done with 200 kW/m² heat flux level and ended after 80 s when the sample collapsed. During the test, no significant aerothermal heating of the sample was observed, i.e. no melting or glowing of the frame material could be seen. The thermocouple measurements, however, showed continuous temperature increases at both the measurement locations between the sample and the holder as well as on the board inside of the housing. Here, the temperature increase was much lower, as the thermocouple was attached to the board whereas the other thermocouples were in contact with the aluminium housing. Due to the high thermal conductivity of aluminium, the temperature gradient was much steeper there.



Figure 4-63: BCM after cover plate removal (left), failing of housing (centre) and board remains just before the end of the test (right)

After about 15 s test time, deformations of the sample can be observed during the rotation. These gradually become stronger and stronger over the test time. After about 70 s test time, tears appear on the back side of the frame and within two seconds, first the cover plate is thrown away and then the remaining frame is ripped apart at the location of the tears. Some parts of the frame remain attached to the sample. The left and centre images of Figure 4-63 show instances where the cover plate is thrown off and the housing breaks. This event

can also be seen by the steep temperature rise. After the housing fails, the test continues for about 8 s. The sample further fragmentates, the remains of the frame and other pieces are thrown off, so that only the board remains left, which sees strong load changes by which it flaps back and forth. Instances later, the fixation of the sample fails. The right image in Figure 4-63 shows the board, strongly bent around the ample holder, shortly before the end of the test.

4.3.1 Model Updates

Although the performance of the 'equivalent metal' GFRP model developed in the SECRET activity appears reasonable, there is some concern as it results in the prediction of undermisable electronics cards. An improved model, with an improved representation of the physical demise processes is required in order to consolidate the demise behaviour of the GFRP material, and to provide increased confidence as to the demise behaviour.

The GFRP model update assessed here is to use the recently developed Simple Balance Integral (SBI) model which has been implemented into SAMj, and applied to both CFRP (COMP2DEM activity) and glasses (COPPER activity). This model allows bulk heating models, such as those used in DRAMA, to include surface energy balance and thermal conductivity effects and thus provide a realistic surface temperature estimate and a representative temperature profile through the material. The GFRP material outgasses as it is a composite material, but where CFRP materials have dry fibres such that the demise is driven by the matrix material, GFRP material demise is driven by the viscosity of the glass fibres. Therefore, the glass SBI model is more applicable to GFRP materials. There are some differences required, however:

- The GFRP outgasses and therefore it may be necessary to account for the blowing of the matrix material.
- Glass materials have very low catalycity to oxygen recombination, but the test results suggest that the catalycity of GFRP materials is higher. It is possible that the initial charring of the matrix and surface melt of the glass produces a lower catalycity surface which causes a reduction in the demise rate. This requires some investigation, and assessment of this effect could be targeted in a static test in the second test campaign.
- The viscosity of the GFRP fibres is not well known, but the demise at 1200°C appears to be consistent with standard soda lime glass materials.

The SAMj Zerodur glass model was used as a starting point for the development of an SBI model for the GFRP material. The temperature data from the BCM tests was used to derive the model in terms of the catalycity of the material and to assess the viscosity as well as demisability. This model differs from the model developed as part of the SECRET activity in both the surface catalycity and the ability for higher temperatures to be reached where the demise is a function of the temperature. This is more physically representative of the processes involved, but the amount of data available is relatively small.

The model derived after the first campaign performed reasonably on the static tests in the second campaign. This demonstrated some important points:

- The catalycity of the GFRP material is consistent across the cards tested, and is higher than that observed for monolithic glass materials.
- The thermal conductivity of GFRP electronics cards varies significantly, and this uncertainty should be included in stochastic analyses.
- The heat to the card material can be reduced due to the electronic componentry on the card. Once the card is sufficiently hot, and the surface sufficiently low viscosity, the componentry is removed easily and the demise of the card continues. This effect is not currently included in the models.
- Componentry is removed from the card at the point that the viscosity is sufficiently low that the card starts to demise. The mass of the electronic components can be removed at this point. Reaching a temperature of 1200°C (1473K) is a good indicator for this.

The dynamic behaviour of the cards suggests that the material becomes very weak, but requires a reasonable force to be applied in order to break the material. Therefore, large GFRP parts may be torn apart if there are more than one large mass attached, but where the GFRP is essentially alone, it would not be expected to fragment. The shape will change, however, and it would be expected that this would increase the ballistic coefficient, but potentially reduce the heated area. Accounting for this in a simple model is not straightforward, and a suitable model has not yet been devised.

The GFRP (glass) model within the electronics models has been updated two ways based on the data from the second test campaign. These are:

- The thermal conductivity has been shown to vary greatly, and this uncertainty is included in the uncertainty analysis, with a uniform uncertainty from 0.025W/mK to 0.1W/mK.
- The removal of the componentry is considered at 1200°C. This is modelled by the fragmentation of a connected-to property at this temperature.

Two types of electronics boxes were assessed, both have the same dimensions. One is a server-type box which is a single module and has a lower overall mass, and the other is a stack-type box which has three modules within it, and a higher overall mass. It is not a simple task to fully understand the difference between these objects, but for the purposes of this modelling effort, the following assumptions were made:

- The external housing is approximately half the mass of the complete electronics box.
- The server-type box contains a rack of electronics cards at approximately 25mm intervals.
 - These are essentially surface-mounted electronics so the mass is driven by the card and the aluminium frames.
- The stack-type box contains a single card within each of the three modules and a more bulky 'power supply' type components.
 - A set of transformers, capacitors and heat sinks is considered on each card.
 - The modules each have a separate aluminium housing.

As there are a number of cards within the box which could be modelled identically, the opportunity has been taken to assess the different material models which have been used for electronics. Thus, for the purposes of this work, cards will be modelled using the SECRET GFRP material, aluminium (current assessment default model) and the glass-based GFRP material in order to understand the differences.

The server-type box model contains the components in Table 4-4. It has a total mass of 18kg. Each of the three card materials is modelled with an aluminium frame, and the remaining six cards are considered as ballast and play no further part in the analysis. Although this is a relatively simple model, it is still significantly more sophisticated, with the use of a GFRP material, a reasonable shape for the card itself, and an aluminium frame, than electronics box models which are used in standard casualty risk assessments.

Table 4-4: Server-Type Electronics Box Model

| Component | Material | Mass (kg) | Notes |
|-----------|----------------------------|-----------|---|
| Housing | Aluminium | 9 | Contains cards 400x300x300mm |
| Card 1 | GFRP (equivalent metal) | 0.5 | Connected to aluminium frame 1 Nested in housing 350x200x3mm |
| Card 2 | Aluminium | 0.5 | Connected to aluminium frame 2 Nested in housing 350x200x3mm |
| Card 3 | GFRP (glass) | 0.5 | Connected to aluminium frame 3 Nested in housing 350x200x3mm |
| Frame 1 | Aluminium | 0.5 | Connected to Card 1 Nested in housing Modelled as single length to allow connection |
| Frame 2 | Aluminium | 0.5 | Connected to Card 2 Nested in housing Modelled as single length to allow connection |
| Frame 3 | Aluminium | 0.5 | Connected to Card 3 Nested in housing |

| Component | Material | Mass (kg) | Notes |
|-----------|----------|-----------|---|
| | | | Modelled as single length to allow connection |
| Dummy | Ballast | 6 | Remaining mass made easily demisable Does not contribute to analysis Required for correct ballistic coefficient of parent |

The stack-type electronics box makes use of the connected-to capability of SAMj. Instead of nesting the card, frames and components separately, the card is considered to be connected to one instance of each component and one instance of the frame. In order to maintain the correct ballistic coefficient, these primary instances of the components/frame act as parents for the remaining instances. This means that the sub-instances of these objects are released at a colder temperature than they should be, but, fortunately, this does not have a significant impact on the results obtained. The model is detailed in Table 4-5.

Table 4-5: Updated Stack-Type Electronics Box Model

| Component | Material | Mass (kg) | Colour | Notes |
|---------------------------|-------------------------------|--------------------------|--------|--|
| Housing | Aluminium | 6 | Cyan | Contains internal housings 400x300x300mm |
| Internal Housing 1,2,3 | Aluminium | 3 | Blue | Contains cards connected to one instance each of componentry, frames Nested in housing |
| Card 1 | GFRP (equivalent metal) | 0.5 | Orange | Connected to Capacitor 1, Frame 1, Heat Sink 1 and Transformer Coil 1 Nested in internal housing |
| Card 2 | Aluminium | 0.5 | Orange | Connected to Capacitor 2, Frame 2, Heat Sink 2 and Transformer Coil 2 Nested in internal housing |
| Card 3 | GFRP (glass) | 0.5 | Orange | Connected to Capacitor 3, Frame 3, Heat Sink 3 and Transformer Coil 3 Nested in internal housing |
| Frame 1,2,3 | Aluminium | 0.0625 (1.0 total) | Purple | Multiplicity 16 – per card (15 instances as child) Connected to Card 1 Nested in housing |
| Capacitor 1,2,3 | Steel | 0.02 (0.4 total) | Cyan | Multiplicity 20 – per card (19 instances as child) Nested in housing |
| Heat Sink 1,2,3 | Aluminium | 0.1 (0.6 total) | Green | Multiplicity 6 – per card (5 instances as child) Nested in housing |
| Transformer Coil 1,2,3 | Copper | 0.15 (0.6 total) | Yellow | Multiplicity 4 – per card (3 instances as child) Contains transformer core Nested in housing |
| Transformer Core 1,2,3 | Iron | 0.35 (1.4 total) | Green | Multiplicity 1 – per coil Nested in transformer coil |

The external and internal housings of the stack are shown in Figure 4-64. The internal components are shown in Figure 4-65. Again, due to the use of multiplicities, a single part of the aluminium frame, a capacitor, a heat sink and a transformer are shown. The left hand frame shows the transformer coils, and the right hand pane shows the nested transformer coil on the bottom card.

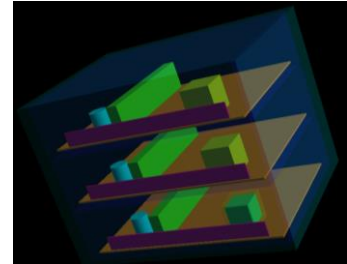
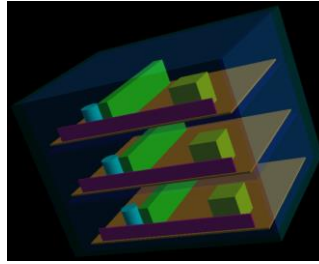
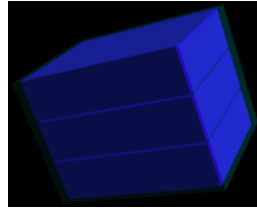
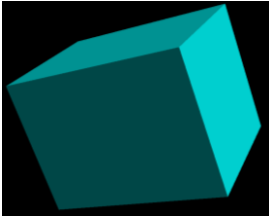


Figure 4-64: SAMj Viewer of Stack-Type Electronics Box Housing and Modules

Figure 4-65: SAMj Viewer of Stack-Type Electronics Box Cards and Internals

4.3.2 Re-Entry Simulations

The server-type electronics box results are shown in Figure 4-66 to Figure 4-67: Landed Mass from Server-Type Electronics Box. The fragment count, and demonstrates that the only objects expected to reach the ground for release altitudes above 75km are the GFRP cards, and this is true for both the improved model and the equivalent metal model. Indeed, for these uncontrolled shallow re-entries, the GFRP models behave essentially the same, which suggests that the equivalent model will be sufficient for DRAMA analyses. This is supported by the landed mass data in Figure 4-67. The mass loss from the GFRP cards is small due to their small ballistic coefficient when released early, and small due to their low demisability when released late. Therefore, there is no good release altitude range to promote demisability. It is important to note that the bending, and potential tearing of the cards is not accounted for, and there is a possibility that they could break-up after the heat pulse is completed. However, from a material demise point-of-view, the GFRP materials will reach the ground in essentially all cases.

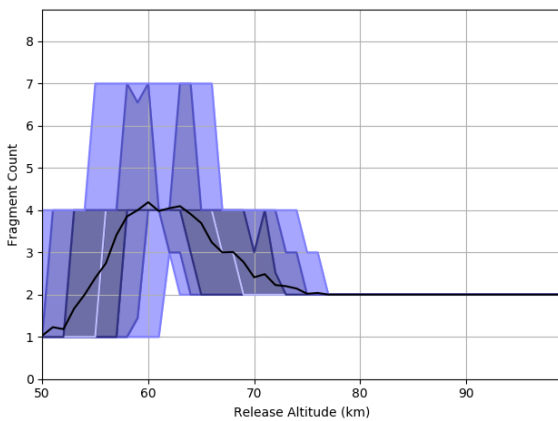


Figure 4-66: Fragment Count from Server-Type Electronics Box

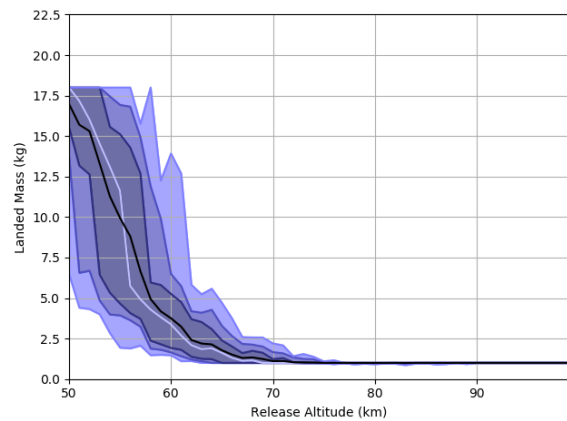


Figure 4-67: Landed Mass from Server-Type Electronics Box

The stack-type electronics box confirms that the new card is slightly less demisable, but the difference between the two GFRP models does not make a clear difference to the results obtained. As with the iteration after the first test campaign, the transformer cores can reach the ground from all release altitudes, and contribute to the higher fragment count at these altitudes as shown in Figure 4-68. These land in the median case at release altitudes below 78km. This demonstrates the importance of relatively early release, as the number of surviving objects becomes large for release altitudes below 70km.

Figure 4-69 confirms that there is a casualty risk at all release altitudes. The important parts are again the GFRP cards, which land in almost all simulations from all release altitudes and the transformer cores. The critical aspect for the analysis of electronics boxes in casualty risk assessments is the behaviour of the GFRP cards. From a material perspective, these will survive re-entry based on the test and rebuilding data from this activity. As they clearly weaken and change shape, it is not clear that they produce the ground risk that these

analyses would predict. Some work on whether further break-up would be seen under aerodynamic force would be required in order to assess this.

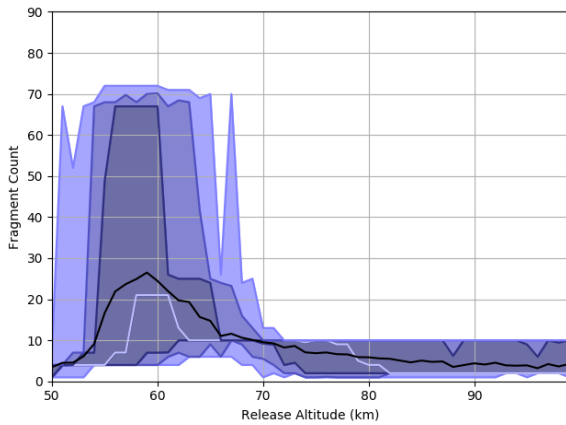


Figure 4-68: Fragment Count from Stack-Type Electronics Box

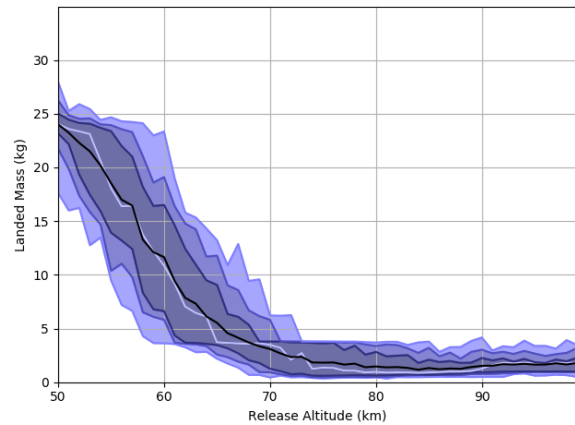


Figure 4-69: Landed Mass from Stack-Type Electronics Box

Overall, the results are very similar to the outputs based on equivalent metal model for the GFRP. This suggests that the equivalent model is sufficiently representative to capture the behaviour of the electronics cards demise in DRAMA analyses.

4.3.3 Modelling Conclusions

The equivalent metal model which was constructed in the SECRET activity is maintained as the most appropriate model for use in DRAMA analyses. For completeness, this is given in Table 4-6. Note that the catalytic recombination coefficient has been reduced in order to match the data obtained in this activity.

Table 4-6: DRAMA Equivalent Metal GFRP Model

| Property | Value |
|-------------------------------------|--------|
| Density (kg/m ³) | 2200 |
| Specific Heat Capacity (J/kgK) | 1046.8 |
| Latent Heat of Fusion (J/kg) | 800000 |
| Thermal Conductivity (W/mK) | 0.15 |
| Catalytic Recombination Coefficient | 0.02 |

The following conclusions can be drawn regarding the modelling:

- Test rebuilding is complex due to the bending of the cards, where shape change but no demise is observed.
- The static material tests provided very good data, and confirm GFRP as a very low demise material, consolidating the models.
- The material model used for the GFRP cards is critical to any casualty risk prediction.
- A new glass-based GFRP material has been developed based on the test data. It is notable that the basic glass models for soda lime glasses were demised too quickly suggesting that the GFRP is highly demise resistant.
- In extrapolation to flight, the existing equivalent metal GFRP model and the new glass-based GFRP model both suggest that large electronics cards will land from any release altitude.
- Although the GFRP material is likely to land, it is currently unknown as to whether it will land in a single part. Where there are two large connected masses (or many, as with the battery module), the material may tear into smaller parts, but a GFRP card is likely to land as a single part, and thus is considered a risk until it can be demonstrated otherwise.

5 RECOMMENDATIONS AND FUTURE WORK

5.1 Star Tracker – Lessons Learned

The star tracker tests have shown that the basic material modelling of the star tracker is good, with the titanium material model performing well in comparison with the test data. Input from Jena Optronik has seen the model of the star tracker consolidated as considering a single titanium part, due to the titanium barrel and focal plane array housing being connected in order to maintain a low and consistent coefficient of thermal expansion (CTE). It has been considered to model two titanium parts, but use of a single part reverts to the model used during the PADRE activity where star trackers were first identified clearly as risk items.

This is complicated by the failure of the test mock-ups in the dynamic tests, where the titanium parts were separated due, it is currently thought, to failure of the helicoils. This has the potential to suggest that the titanium parts may be separated, and some type of fragmentation model could be considered for the bolted joints. However the usage of helicoils in the mock-ups tested is not consistent with current flight models. At this stage, this phenomenon is not sufficiently well understood to be included in modelling of bolted joints with helicoils in destructive re-entry risk analyses, but is clearly an area where future investigation is necessary.

The melting of the glass in the Jena Optronik unit was also of particular interest. This demonstrated that the glass used in the star tracker was not fused silica, which is a very high temperature material and would not have shown signs of melt at the temperatures reached. The flow of the material due to its reduced viscosity at the test temperatures suggests that the glasses within the star tracker were similar to borosilicate glasses in terms of demisability. There were a number of lenses of different grades within the unit, but only the barrel cover glass was identified as borosilicate pre-test. It is interesting to note that none of the glass was retrieved from the test. This suggests that testing of a range of glass materials should be performed in order to construct a set of demise models which can be used for optical units in both platform and payload analyses.

Due to the titanium barrel, star trackers remain a potentially critical item, and should not be modelled in casualty risk analyses without considering the titanium part. Larger star trackers should be expected to always pose a ground risk, where smaller star trackers have a reasonable probability of demise.

5.2 Batteries – Lessons Learned

The battery tests consolidate the modelling of ABSL cells via a modified steel material model as the demise is again demonstrated to be driven by the behaviour of the steel can. The demise of single ABSL cells can now be considered well-established.

The fragmentation of the battery module has been clearly shown to be driven by the failure of the GFRP material, and that this fragmentation is enhanced by rotational motion. Therefore, these tests suggest relatively clearly that a reasonably fast fragmentation of an ABSL battery module can be expected. However, the fragmentation is not instantaneous, and thus it is important that a GFRP layer should be included in the model. As the GFRP is torn into small parts as the cells are removed, the GFRP should not be considered as a ground risk even though it is expected that the material will reach the ground.

Unfortunately, it was not possible to test other, notably SAFT, cells within this activity. Although the demise behaviour of other cells is expected to be similar to the ABSL cells as they are chemically similar, this should be confirmed by test. This is particularly important as the larger cells are predicted to be less demisable, and therefore a larger casualty risk. With the potentially large number of cells in a spacecraft battery, this can make a significant contribution to the risk.

The simulations suggest that there is a limited risk from batteries using ABSL cells, mainly driven by the small size of the cells. As the cases in which cells land have a high risk due to large numbers of landed objects, a median assessment is not suitable for batteries, and some casualty area budget should be allocated to batteries. In general, the risk will be relatively low (but non-zero) for these types of batteries for a release altitude above 80km.

5.3 Electronics – Lessons Learned

The demise behaviour of the electronics cards is not easy to assess. The GFRP material, which is reasonably standard across all electronics cards, is a very low demisability material, but becomes very weak at high

temperature. It is useful to note that the most common GFRP material used in spacecraft electronics is the same FR4 material which is the most popular material for terrestrial applications. Therefore, it is easy to obtain samples of material which are relevant to spacecraft application.

The material behaviour is complex. The tests demonstrate that the material becomes soft at relatively low temperatures, and can be bent and twisted by relatively low mechanical forces. Where there is a substantial mass on the material, it is possible that this may induce a tearing of the material, as observed with the breaking of the sample from the sample holder. However, where there is no major mass on the material, it is likely to change shape, but there is no evidence that the material will fragment into small pieces which do not pose a ground risk.

The static tests in the second campaign were designed specifically to consolidate the thermal material demise model for the GFRP. This has been successfully achieved, and demonstrates a small decrease in the demisability of the GFRP material relative to the model devised in the SECRET activity. The previous proxy model is considered sufficient for use in DRAMA casualty risk assessments.

The balance integral glass model used in SAMj has been applied to the GFRP material, and the results have demonstrated that the model is appropriate, and that the GFRP is of a similar demisability to glass materials such as Zerodur, and is less demisable than standard borosilicate glass. The tests also demonstrate that the GFRP is a low catalycity material, but the results suggest that it has a higher surface catalycity to molecular recombination than pure glass materials.

Extrapolation to flight of the thermal model suggests that the GFRP will reach the ground from essentially all release altitudes, which is consistent with the findings from both the SECRET activity and the PADRE activity. This suggests that electronics material poses a ground risk, and some evidence that the GFRP material breaks up would be required in order to suggest otherwise.

Furthermore, the work done in this activity suggests that large electronics components, such as transformers, can pose a ground casualty risk, and should not be ignored in casualty risk assessments.

5.4 Modelling

5.4.1 Model Construction

Within this activity, four specific material models have been assessed and the data delivered for inclusion in the ESTIMATE database. These are given in Table 5-1. Of most importance is the finding that glass material surfaces are very low catalycity. This reduces the heat input to these surfaces, reducing their demisability. This effect is less severe, but still important for GFRP materials.

Table 5-1: Material Model Updates

| Material | Notes |
|---------------------|--|
| Titanium | Current DRAMA material model good – included as consolidation |
| Battery Cell | Modified DRAMA steel material model to capture battery cell behaviour. Uses a reduced latent heat. |
| GFRP | Balance Integral Model: utilised in SAMj. Based on viscosity driven glass material demise models developed within the COPPER activity. |
| GFRP Proxy | Equivalent metal GFRP proxy model. Suitable for DRAMA, and consistent with the model recommended from the SECRET activity. |

The star tracker recommendations are given in Table 5-2.

Table 5-2: Star Tracker Model Recommendations

| Component | Notes |
|---------------------------|--|
| Housing | Aluminium. A single aluminium component can be used for the entire housing, or separate components can be considered for the barrel and housing. Where separate components are used, the barrel can be connected-to, otherwise it should be contained-in. Failure of the housing is preferred to be via a mass loss model (not currently available in DRAMA). Removal of housing at full demise is preferred to removal at melt temperature in a DRAMA-compatible model. |
| Barrel/Focal Plane | Titanium. The recommendation is to model this as a single titanium part, or as a collection of connected titanium parts with undemisable joints. The latter is used to capture the length scales of the model, as shown in Figure 5-1. |
| Lenses | Borosilicate glass. It is preferred that these are modelled using a balance integral approach (not currently available in DRAMA). Proxy 'equivalent metal' glass models can be acceptable, but must be demonstrated by test. |

An example of a star tracker model with separate baffle and housing, and a multi-part titanium barrel is shown in Figure 5-1. Note that the focal plane housing (pink) is also titanium and is connected to the barrel with an undemisable joint.

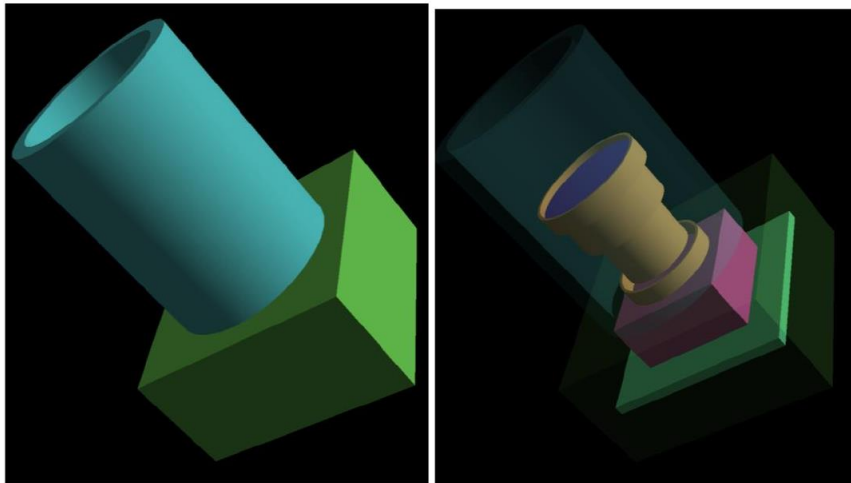


Figure 5-1: Star Tracker Model Example

The battery model recommendations are given in Table 5-3.

Table 5-3: Battery Model Recommendations

| Component | Notes |
|----------------|---|
| Housing | Aluminium. A single housing is recommended for the whole battery. This is recommended to fail using a mass loss model (not currently available in DRAMA). The remainder of the battery components are contained-in the housing. |
| Module | GFRP. The battery should be separated into a number of modules which are representative of the architecture. Each of these modules should be modelled as GFRP (preferably a balance integral material, but a test-validated proxy is acceptable), and the |

| Component | Notes |
|--------------|---|
| | correct total mass of GFRP should be considered. This is also recommended to fail using a mass loss model. The cells are considered as contained-in the GFRP modules. A suitable multiplicity can be used for identical modules. |
| Cells | Steel Proxy Material. The cells should be considered as contained-in the modules with a suitable multiplicity for the cell number. The test-validated battery cell proxy material should be used for the cells. This is currently applicable to all cells, although has only been validated for ABSL cells. |

The nesting of the modules inside the housing, and the cells inside the modules is shown for three different cell sizes in Figure 5-2. Note that the multiplicity is used for two identical modules and for the cells.

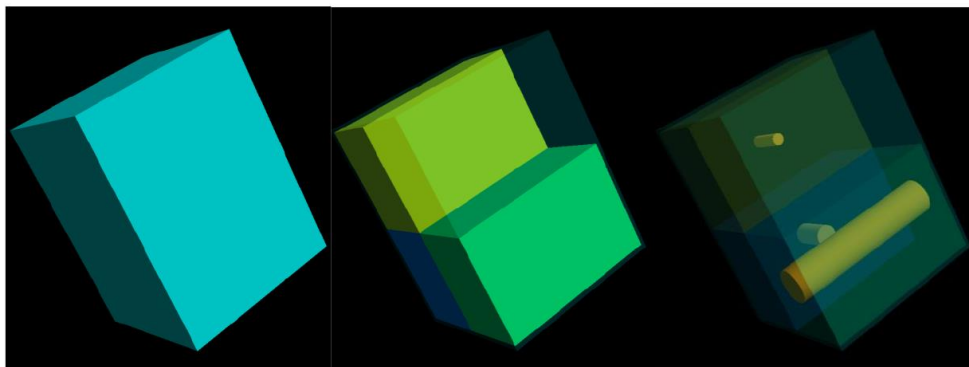


Figure 5-2: Battery Model Example

The electronics model recommendations are made based on the evidence from the testing, and are given in Table 5-4. It is acknowledged that this provides a very low demisability material for electronics cards, however, the material is expected to survive thermally, but becomes mechanically weak at elevated temperature.

Table 5-4: Electronics Model Recommendations

| Component | Notes |
|-------------------------|---|
| Housing | Aluminium. A single housing can be used for the whole electronics box. This is recommended to fail using a mass loss model (not currently available in DRAMA). The remainder of the electronic components are contained-in the housing. Where a stack-type electronics box is used, and there is an internal housing separating the electronics into similar units, this can be modelled as a multiplicity, in which case it is more efficient to model the inner housing as well. Failure of the inner housing is again recommended to be modelled using a mass loss model. |
| Electronics Card | GFRP. The GFRP card should be modelled with the correct mass of GFRP, which is expected to be approximately half the mass of the card, frame and componentry unless large components are present. If the componentry is small, it is acceptable to neglect their modelling. The GFRP is preferred to be modelled using a balance integral model (not currently available in DRAMA), but a test-validated 'equivalent metal' proxy model is acceptable. |
| Frames | Aluminium. This can be modelled in two ways. Either as a connected-to part, which is a single part representative of the frame length scale. To do this, the thickness and height of the frame should be represented, but the length should be a total length of all the frame |

| Component | Notes |
|--------------------------------------|---|
| | <p>attached to the card. This should be released using a mass loss model (not currently available in DRAMA). Alternatively, model as contained-in the GFRP as this maintains the ballistic coefficient of the card giving a more reasonable opportunity to demise. In this case multiple lengths of frame can be modelled using multiplicity.</p> <p>Note: DRAMA will currently disregard the parent component (card) at the point the children are released. This needs to be fixed in future versions to make use of the release capability reliably.</p> |
| <p>Electronic Componentry</p> | <p>This is recommended to be modelled when a large electronic component, such as a transformer is present on an electronic card. It is preferred that this component is connected-to the card. Where there are multiple similar components, these are more efficiently modelled as a multiplicity, in which case they must be considered contained-in the card. Release of the componentry is recommended at a card temperature of 1200°C however modelled.</p> <p>Note: DRAMA will currently disregard the parent component (card) at the point the children are released. This needs to be fixed in future versions to make use of the release capability reliably.</p> |

An example electronics box with three electronics cards with attached componentry is shown in Figure 5-3. The purple object is an aluminium frame which is representative of a contained-in multiplicity item.

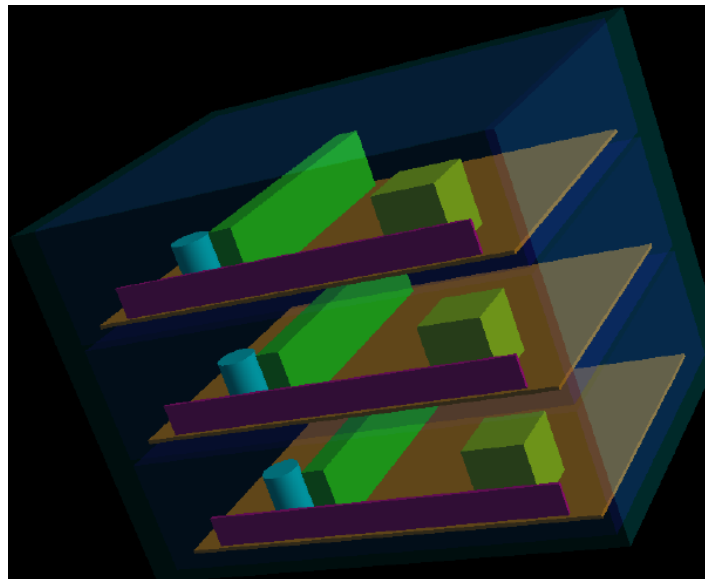


Figure 5-3: Electronics Box Model Example

5.4.2 Required DRAMA Upgrades

The above model descriptions require three upgrades to DRAMA. These have all been proposed previously in other activities, thus this work consolidates the need for these models to be included in DRAMA.

Balance Integral Glass Model

The balance integral model as developed during the COPPER activity is recommended for inclusion within DRAMA. Although it is possible to construct equivalent metal proxy models which can capture test data, extrapolation to other materials cannot be performed, and there is a limit on the reliability of the model as it is

constructed strictly for the conditions tested. The recession rate change with temperature cannot be fully captured using a fixed temperature and latent heat as this is not a true reflection of the material behaviour.

The balance integral model respects the physics of glass demise in that it models the reduction of viscosity with temperature and thus captures the speed at which the material can be removed from the surface giving a recession rate which is a function of temperature. As well as GFRP cards, the use of borosilicate glass in the star tracker suggests that a fused silica model (essentially undemisable) is not suitable for all optical glasses, and that there is benefit in modelling glass materials well as some of them can demise.

As there is a large range of glass materials, and viscosity data is available for a number of grades of glass materials, a basic model can be constructed using the balance integral model, which can then be confirmed by testing.

Mass Loss Model

A mass loss criterion, where a certain event can be triggered when the mass of a component reaches a fraction of the original component mass is recommended for implementation. A mass loss criterion can be utilised in DRAMA for a number of purposes:

- Criterion for fragmentation. This provides a method of predicting fragmentation when an object is partially demised, where there is no current method of selecting a criterion between melt temperature and complete demise. These two criteria can provide significantly different results, and a more flexible method would be useful. This is used as standard in SAMj simulations as it is reflective of test observations.
- Criterion for child release. This allows covering of the realistic case where the children of a component are released when the component is partially demised.

A stochastic method is recommended for use with this criterion as there is clearly a significant uncertainty associated with it. It is also worth noting that the mass loss criterion does not need to be restricted to mass loss by melt, but can also result from mass loss by active oxidation, for example.

Reschedule Parent Object as Default

A critical issue with the current version of DRAMA is that a parent object is considered demised when children are released, even when the parent object has significant remaining mass. This is an issue, as, for example, componentry cannot be considered as a child of an electronics card, as on the release of the componentry (1200°C would be the recommended temperature), the card is considered demised. As the card is likely, based on the material model, to reach the ground, this is an issue with the current model in DRAMA.

Indeed, this can be currently used as a method to remove risk items from the DRAMA results as a CFRP object which releases children on a given condition will be removed from the results on child release. As CFRP objects are undemisable in DRAMA, this would result in this CFRP item not being predicted to be a risk object when the DRAMA model would predict it, were it not a parent object, to reach the ground intact.

Rescheduling of the parent object within the simulation framework becomes more important when used in conjunction with the mass loss model approach, as there will be many more cases of child objects being released where there is a significant mass of the parent remaining.

5.4.3 DRAMA Models

The recommended models of Section 5.4.1 cannot all be achieved in DRAMA. This section provides an overview of compromises necessary to construct a representative model with the current DRAMA capability.

The DRAMA star tracker model differs from the SAMj model in two ways. Firstly, the GFRP material model is the equivalent metal proxy model, and secondly, the mass loss failure criterion for the aluminium parts is not considered. The borosilicate glass model used within SAMj should be mapped to a Zerodur model in DRAMA as this is the closest available model.

Regarding the modelling of batteries, the differences from the SAMj model are again in the GFRP material model and the mass loss criterion. In SAMj a mass loss criterion is used for both the housing and the GFRP module failure, which result in the release of the children. This is delayed to full demise in the DRAMA model.

The electronics box is more difficult to model in DRAMA due to the inability to release child items with the parent remaining an object in the simulation. It is expected that this will be fixed in future releases of DRAMA.

The current recommendation for the modelling of the electronics in DRAMA is to model the housing, and inner housing (if present), and to model the remaining mass as GFRP cards. Multiplicity should be used to represent the card number. This will overstate the landed mass as the cards contain componentry and have aluminium frames which are not accounted for.

Once DRAMA has the capability to reschedule a parent object, it is recommended to model the card as being connected to the frame (one part representing the whole frame) and containing the componentry, which is released at 1200°C. The frame has no fragmentation criterion, but would be released based on a mass loss criterion once this is available in DRAMA.

5.5 DIVE recommendations

This activity has served to consolidate the findings from the SECRET activity on the demisability of batteries and electronics cards, and has also provided test support for the expected behaviour of star tracker internals. There were no major surprises in the testing, and only small modelling changes have been required to capture the data.

Importantly, the process of testing and modelling has followed the existing DIVE procedures and has demonstrated that, for assessing component demisability, the guidelines have performed well. As with previous campaigns, the critical aspects for assessing the demise of a component are:

- Fragmentation
- Input heat flux
- Material properties

Successful use of the stepped heat flux approach has again been demonstrated, and this is highly recommended to determine demise / no demise thresholds for equipment.

In this activity, dynamic testing has also been used. There are benefits to using dynamic tests, as this has shown enhanced fragmentation for the battery modules, and highlighted a potential fragmentation process with bolted joints using helicoils, which require further assessment. However, the tests are more difficult to understand. It is important to note that modelling using an average heating condition has been found to be adequate in the test rebuilding, and that this is acceptable for future campaigns.

The tests on the electronics cards were difficult to assess due to the change in shape, and thus heating profile, on the cards. This resulted in the second test campaign being changed to provide two extra static tests on the cards, which had a backing structure in order to prevent shape change, in order to provide a consolidated material model for the GFRP. These material tests are considered to be of very high value, and significantly increase the confidence in the material model.

Specific recommendations for testing and modelling are:

Testing:

- Simple material tests should be performed for all materials not currently in the ESTIMATE database. These tests should be performed in a representative facility, in a static condition, and with the material backed by the sample holder to prevent shape change. More than one test condition (can be stepped conditions from the same test) is mandatory.
- Where the material is part of the component (such as the battery can), a static test is sufficient, and is required to be rebuilt. More than one test condition (can be stepped conditions from the same test) is mandatory.

Modelling:

- Star tracker models are recommended to contain one titanium part. The geometry can be accounted for by modelling multiple titanium parts with undemisable joints.
- Battery models should include a GFRP layer. The recommended GFRP material proxy model is acceptable for use. GFRP reaching the ground should not be included in the casualty risk in this specific case.
- GFRP electronics cards are unlikely to demise, but are likely to remain contiguous and thus pose a ground risk. Further testing is needed to demonstrate whether these cards will disintegrate through peak dynamic pressure which occurs later in the trajectory.

5.6 Recommendations for Future Work

5.6.1 Testing and Modelling

From this activity, there are a number of recommendations for further testing. These include:

- Investigation into demisable electronics cards materials

This activity consolidates the findings from both SECRET and COMP2DEM that GFRP materials are low demisability and can provide a significant ground risk. Given that electronics are prevalent on spacecraft, this poses a major issue. It is proposed, therefore, to perform an activity to assess other electronics materials in order to determine whether there are alternative, demisable materials which could be used for spacecraft electronics where the satellite is expected to re-enter.

- Investigation into the fragmentation due to failure of bolted joints with helicoils.

The star tracker mock-up were observed to fail in the dynamic testing due to pull-out of the bolts. This is thought to be related to the use of helicoils. Investigation of the temperatures required for helicoil failure, the force required to remove the screws (related to object mass in ground testing) and the behaviour of different helicoil materials is recommended. This could have a significant impact in fragmentation modelling of large parts, and could also be used to promote fragmentation in order to improve demisability.

- Construction of a glass material demisability database (within SCORED)

The melting of all the glass materials from the star tracker was not expected, as some were thought to be fused silica. As the grade of glass appears to be lower, even for optical instruments, it is recommended to test a range of glass materials with different viscosity profiles.

It is suggested that this database be housed within the SCORED database. With a validated physical modelling approach, it would then be possible to perform a relatively cheap viscosity measurement in order to gain the demisability data required for the modelling of further glass materials.

- Testing of larger battery cells

The recommended battery models are based on the testing of ABSL cells. There are other, larger cells used on spacecraft, including the SAFT cells which were intended to be tested within this activity. It is important to determine the whether the demise behaviour of the larger cells is also determined by the behaviour of the steel can as these cells are much more likely to pose a ground casualty risk.

- Assessment of potential GFRP material disintegration in re-entry

As the GFRP cards survive from a material perspective, but become soft at high temperature, there is a possibility that they might disintegrate under higher pressures. This is not considered a high likelihood, but this would remove some of the difficulties associated with the casualty risk from GFRP cards which would be predicted using the results from the testing performed in this activity (and also within SECRET and COMP2DEM). This testing would need to be performed in a high temperature facility with forces applied to hot cards. A wind tunnel is not necessary, a static facility would be sufficient.

5.6.2 Design Ideas to Improve the Equipment Demise

Optical and electronic equipment for spacecrafts is design to fulfil a certain function in the operational environment and constraints. It must be able to fulfil its performance requirements derived from the mission and system design in space environment while at the same time conforming to constraints imposed by ground preparation, launch and budgets.

The main design requirements and constraints for equipment concern:

- Function and Performance
- Mass, Volume and Accommodation
- Operational Environment
- Power Budgets
- Launch Loads

Currently the demisability of the equipment during atmospheric re-entry often is still an afterthought in the design. Usually, the design focus on improvement of performance, reduction of mass and volume as well as

power demands. Although more and more equipment suppliers also acknowledge the need for demisable equipment. However, the design requirements resulting from demisability often entail change of materials and/or design modifications that are difficult to align with performance requirements and requirements in the other areas listed above.

Nevertheless, the following sections aim to summarise possible ideas for starting points and design approaches to improve the demisability where needed. However, no in-depths analysis of the feasibility and impacts can be provided at this point as it is beyond the scope of this activity and is better tackled in dedicated follow-up activities.

Star Trackers

Due to their function the imaging systems of star trackers are always located at the outside of the spacecraft. Therefore, they are exposed early on to the re-entry flow. However, as they are made of hard to demise material the results of this activity showed the especially larger star trackers still pose a causality risk. This leaves three potential areas for demisability improvement:

- Change of materials
- Reduction in overall size
- Early separation of the imaging systems

All of these might be difficult to achieve without impairing in the performance and / or the system compatibility of the star trackers. Star trackers are essential sensors for GNC and AOSC of spacecraft. To fulfil their function a high accuracy and thereby thermal stability of the imaging system is needed. Accordingly, titanium is often selected as material for the lens tube and focal plane housing. In addition, titanium is light weight, which is beneficial for the mass budget, as usually three star trackers are present on a spacecraft. Therefore, the change to another more demisable material is not straightforward and requires careful investigation.

Although star trackers are available in different sizes, they differ in performance and accuracy. Small star trackers (< 300 g) are usually based on heritage but are optimized and adapted for cost driven design and mass production. They are used mainly in small sat constellations and for applications that require a lower accuracy in terms of position knowledge. However, a significant reduction of the overall size of the star tracker imaging system is not feasible for application where higher accuracy is required.

In case of early separation of the imaging system into small parts it needs to be ensured that the parts demise or fall below the casualty threshold of 15J. The lens tube and focal plane housing are the most massive parts of the imaging system. Even if separated they may still pose a risk in case of larger star trackers. So, separation maybe be counterproductive. The small parts include lenses and electronic components which may fall below the threshold as they have a very low mass of a few grams. In any case further investigation is required to determine the effectiveness of early separation. In case early separation is effective, demisable inserts or helicoils could be incorporated in the design.

Batteries

The activity showed that demisability of battery packs using small individual cells is already good. Therefore no further improvements are proposed at this point. The demisability of battery pack comprising larger individual cells may pose a risk, and need to be investigated further.

Electronics Cards

The activity showed that the GFRP material, which is used as a base for most electronics cards, is a very hard to demise material although it becomes mechanically very weak at high temperatures. As first iteration three potential approaches for demisability improvement come to mind:

- Change of base material
- Size reduction of large cards
- Fragmentation / break up of large cards

The change of the base material from GFRP to different more demisable material seems like an obvious solution. However, the material is widely used because of its technical and cost advantages. It a composite material composed of woven fiberglass cloth with an epoxy resin binder. It is standard for space and terrestrial applications and it currently hard to replace. As an intermediate solution, the feasibility of the more frequent use of polyamide-based PCB for certain electronics cloud also be investigated in a future activity.

But a more sustainable solution may become available in the future from current research to make the design of electronic cards more ecofriendly. The research is focusing on paper-based PCB without the use of glass fibers or epoxy. The research ranges from using treated "normal" paper to specifically engineered cellulose nanofibers as base material. First production efforts were already successful; however, the technology is currently not yet advanced enough for complex electronic boards as used in computers. In any case, further investigation is required to determine the feasibility of paper-based electronic boards for space applications and their potential advantages in terms of demisability. In case they would prove feasible for space application, it would also significantly improve the environmental impact of the spacecraft life cycle.

The size reduction and/or fragmentation of electronic cards to accomplish the predictable separation into small pieces that do not pose a risk is conceivable, yet very impractical at this point. This would require, for example, significantly more connections or some sort of predetermined breaking points. Both are difficult to align with functional and mass/volume requirements. Another approach to facilitate the break-up of large cards could be to change the layout and arrangement of fiberglass cloth to implement breaking points, but also this is similarly difficult to align with functional requirements and environmental constraints.